



TAMPEREEN TEKNILLINEN YLIOPISTO
TAMPERE UNIVERSITY OF TECHNOLOGY

MIRVJEN OLLONI

COMMISSIONING OF 6 MV FFF PHOTON BEAM FOR SBRT
LUNG TREATMENTS

Master's thesis

Examiners: Maunu Pitkanen, Mika
Kapanen, Hannu Eskola.
Examiner and topic approved by the
Faculty Council of Natural Sciences
on 8th of May 2013.

ABSTRACT

TAMPERE UNIVERSITY OF TECHNOLOGY

Degree Programme in Biomedical Engineering

OLLONI, MIRVJEN: Commissioning of 6 MV FFF beam for SBRT lung treatments

Master of Science Thesis, 76 pages

August 2013

Major subject: Medical Physics

Examiners: Maunu Pitkanen, Mika Kapanen, Hannu Eskola

Keywords: flattening filter free (FFF), stereotactic body radiation therapy (SBRT), volume modulated arc therapy (VMAT), gamma analysis.

The use of stereotactic body radiation therapy (SBRT) for lung treatments is very popular in radiotherapy clinics. This is because of its better results compared to the other treatments. The development of flattening filter free (FFF) beams has given a new perspective to this treatment. In this thesis, the commissioning of SBRT FFF beam for central lung treatment was aimed.

Two spherical volumes of diameter 3 cm (PTV 3) and 6 cm (PTV 6) representing the planning target volumes were created within the central lung area in Alderson phantom. The dose plan for the treatment was done for 6 MV FFF photon beam using stereotactic radiotherapy (SRT) volume modulated arc therapy (VMAT) and dose fractions of 4 Gy, 7.5 Gy, 11 Gy and 18 Gy. Dose distribution calculations were performed in Eclipse treatment planning system (Varian Medical Systems, Palo Alto, CA). Radiation Therapy Oncology Group (RTOG) protocol was utilized to obtain the required dose conformity within the target. Dose plan verification was done by ionization chamber matrix detector (in two different setups: combined with the cubic solid water phantom and mounted in the gantry) and radiochromic film inserted within the cubic solid water phantom. Irradiation was done with Varian TrueBeam STx linear accelerator (Varian Medical Systems, Palo Alto, CA).

Results of dose conformity were checked using dose-volume histograms (DVH) and were in accordance with the RTOG protocol. Moreover, measured and calculated dose distribution data were compared using gamma analysis with the acceptance criteria of 3 %, 3 mm. According to the suggested criteria (less than 5 %) of technical reports series (TRS) 398, the general average values of the disagreement between measured and calculated data obtained from the ion chamber matrix detector for PTV 6 were within the required limits, 4.2 % for both of the detector setups. However, this was not the case for PTV 3 because the general average values were 6.2 % and 6.5 % for each of the detector setups. Main reasons for these unacceptable results were mostly due to the small field sizes and poor resolution of the matrix detector. Film measurements showed very satisfactory results regarding the shape of the measured dose profile compared to the calculated one. The only problem with film results was the unacceptable absolute dose difference between these two dose profiles, approximately 10 %, which most likely was due to inaccuracies from film calibration or post processing.

Based on those results, it was concluded that the commissioning of the 6 MV FFF photon beam for SBRT lung treatment was partly successful. Before its clinical application, further studies are needed related to the mentioned dosimetric uncertainties.

PREFACE

Commissioning of FFF 6 MV beam for SBRT lung treatments with the VMAT technique has been performed at the department of radiation therapy at Tampere University Hospital, Finland and it has introduced interesting challenges and satisfaction during the past half a year. I gained important knowledge from the field and a very valuable working experience. These were possible from the direct or indirect contributions of many people who I would like to thank.

First and for most, I would like to thank my dear parents, Dana and Gezim for their immense support on my education; love and care they have provided to me. I will be always grateful to them. Also, special thanks go to my twin Tiku and to my uncle Uran for being always supportive.

Maunu Pitkanen and Mika Kapanen, thank you very much for your supervision during my thesis work at the department. Thanks to you I have enjoyed my topic, learned a great deal about radiotherapy and improved my skills to do research more efficiently and professionally. I do appreciate your willingness to help and answer every question I brought up even in your busiest times. It has been a great pleasure and privilege to work under your supervision. In addition, many thanks go to Antti Vanhanen and Evaa Boman for their advices and the help they have offered. I also would like to thank Mr. Hannu Eskola for offering me the topic and the opportunity to work at the TAYS radiotherapy department.

Finally, I would like to thank my friends whom I met in Finland for making my stay here unforgettable. Special thanks go to Artur, not only as my best friend but also for being a great person to work with. Last but not least, thank you to Baca, Amalia, Borja, Defne and Saeed for all the fun times in the past two years.

Tampere, September 2013

Mirvjen Olloni

LIST OF SYMBOLS

ϕ_β	homogeneous photon flux in the beamlet's cross-section
$\rho(\tilde{x}, \tilde{y}, \tilde{z})$	electron density
ρ_{water}	electron density of water
$\gamma(r_m)$	pas-fail criteria for gamma analysis
$\delta(r_m, r_c)$	distance-to-agreement equation used for gamma analysis
ΔD_M	threshold value to pass the dose criteria
Δd_M	threshold value to pass the isodose distance
$CBSF(x, y)$	collimator backscatter factor for open field
$D(\tilde{x}, \tilde{y}, \tilde{z})$	dose calculated from the energy conversion
$D_c(r_c)$	calculated dose at r_c
$D_m(r_m)$	measured dose at point r_m
$D(r_m + r)$	distance between a measured dose point and the closest calculated dose point within the r distance
D_{calib}	value of reference dose at calibration depth
$D_{norm}(x, y)$	dose calculated at the field normalization point
D_{ref}	calculated dose from AAA at the calibration depth for the reference conditions
$E(\tilde{x}, \tilde{y}, \tilde{z})$	total absorbed energy at any voxel within the patient (in 3D)
$E_{cont, \beta}(\tilde{x}, \tilde{y}, \tilde{z})$	energy generated from electron contamination source
$E_{ph, \beta}(\tilde{x}, \tilde{y}, \tilde{z})$	photon energy at beamlet β
$E_{ph1, \beta}(\tilde{x}, \tilde{y}, \tilde{z})$	energy generated from primary photon source
$E_{ph2, \beta}(\tilde{x}, \tilde{y}, \tilde{z})$	energy generated from secondary photon source
f_0	start dose
f_∞	end dose
$f(x)$	normal tissue objective function
$I_\beta(z')$	energy deposition density function in z-direction
$I_\beta(z, \rho)$	energy deposition density function
$K_\beta(x, y, z)$	scatter kernel
MU_{calib}	value of reference dose in MU at calibration depth
MU_{norm}	monitor units calculated at normalized point
r_c	spatial location of the calculated distribution relative to the measurement point
r_m	position of a single measurement point
$(\tilde{x}, \tilde{y}, \tilde{z})$	relative position of (x, y, z) with regard to the origin of the beamlet coordinate system
$WCF(x, y)$	wedge correction factor
Z'	radiological depth

LIST OF ABBREVIATIONS

1D	one-dimensional
2D	two-dimensional
3D	three-dimensional
4D	four-dimensional
3DCT	three dimensional computed tomography
3DRT	three dimensional radiotherapy
4DCT	four dimensional computed tomography
AAA	anisotropic analytical algorithm
ADC	analog-to-digital converter
BEV	beam's eye view
CAX	central axis
CP	control points
CT	computed tomography
CTV	clinical target volume
DICOM	digital imaging and communications in medicine
DMLC	dynamic multi-leaf collimator
DTA	distance-to-agreement
DVH	dose-volume histogram
DVO	dose volume optimizer
FF	flattening filter
FFF	flattening filter free
GTV	gross target volume
HU	Hounsfield unit
IGRT	image guided radiotherapy
IMAT	intensity modulated arc therapy
IMRT	intensity modulated radiotherapy
ITV	internal target volume
Linac	linear accelerator
MCube	MULTICube Lite solid water phantom
MLC	multileaf collimator
MRI	magnetic resonance imaging
MU	monitor unit
MXX	MatriXX ^{Evolution} detector
NSCLC	non small cell lung cancer
NTO	normal tissue objective
OAR	organ at risk
PET	positron emission tomography
PGO	plan geometry optimization
PRO	progressive resolution optimizer
PTV	planned target volume

RF	radio frequency
ROI	region of interest
RTOG	radiation therapy oncology group
SBRT	stereotactic body radiotherapy
SPECT	single photon emission computed tomography
SSD	source-to-surface distance
TPS	treatment planning system
TRS	technical report series
VMAT	volume modulated arc therapy
Z	atomic number

CONTENTS

1.	Introduction.....	1
2.	Theoretical background.....	2
2.1.	Treatment of cancer.....	2
2.2.	Medical Linear accelerator (linac).....	3
2.2.1.	Brief history of linac.....	3
2.2.2.	Modern linac.....	5
2.3.	Clinical Radiotherapy.....	7
2.3.1.	Clinical structure definitions.....	7
2.3.2.	3DCRT.....	8
2.3.3.	IMRT.....	9
2.3.4.	VMAT.....	11
2.3.5.	SBRT.....	13
2.4.	FF vs. FFF beams.....	15
2.4.1.	Advantages of FFF beam.....	16
2.4.2.	Limitations of FFF beam.....	17
2.5.	Treatment Planning System.....	18
2.5.1.	Principles of radiotherapy treatment planning system.....	18
2.5.2.	Analytical Anisotropic Algorithm.....	19
2.5.3.	Optimization of dose distribution.....	23
2.6.	Aims of the thesis.....	25
3.	Materials and Methods.....	26
3.1.	Target contouring.....	26
3.2.	Dose planning.....	27
3.3.	Optimization of dose distribution.....	28
3.4.	Plan evaluation and verification.....	29
3.5.	Dosimetric Verifications.....	30
3.5.1.	Matrix detector on treatment couch.....	30
3.5.2.	Matrix detector mounted on treatment head.....	32
3.5.3.	Film measurement.....	33
3.6.	Dose distribution evaluations.....	36
4.	Results.....	39
4.1.	Calculated dose distributions.....	39
4.1.1.	Delivery time and the amount of monitor units.....	42
4.2.	Dosimetric verifications.....	43
4.2.1.	Matrix detector on treatment couch.....	43
4.2.2.	Matrix detector mounted on treatment head.....	47
4.2.3.	Film measurement.....	52
5.	Discussion.....	54
5.1.	Dose within the target volume.....	54
5.2.	Delivery time and monitor units.....	55

5.3.	Dosimetric verifications with matrix detector.....	55
5.3.1.	Matrix spatial resolution and field size	56
5.3.2.	Angular dependency and other factors.....	57
5.3.3.	Future work	58
5.4.	Dosimetric verifications with film measurements.....	60
5.4.1.	Future work	61
6.	Conclusion.....	62
7.	References	64

1. INTRODUCTION

External radiotherapy is the most common treatment procedure used in oncology. It uses one or more external photon beams to treat the tumor inside the patient from outside the patient's body. Its aim is the tumor necrosis by delivering a high dose of radiation to the malignant tissue site and sparing the surrounding healthy tissues as much as possible. In other cases it is also used for palliative purposes rather than curative ones. [1.] Today there are many techniques utilized to deliver the photon beam to the patient with the main ones being three-dimensional conformal radiotherapy (3DCRT) and intensity modulated radiotherapy (IMRT) and volume modulated arc therapy (VMAT); all very useful for stereotactic body radiotherapy (SBRT) treatments. SBRT, which is in the focus of this work, differs from other treatments because of its higher accuracy and the use of high radiation doses in only few fractions. Its implementation started about 20 years ago and with the further development of computing technology it became a more common technique in radiotherapy [2]. It is used for many tumor sites but most commonly for lung treatments [3].

The development of flattening filter free (FFF) beam is thought to give further advantages to SBRT. The main benefit offered from FFF beam is the possibility of using much *higher dose rates* and therefore a *shorter delivery time*. Reducing the delivery time would keep the patient on the treatment couch for a shorter period. Thus, giving more comfort to the patient and decreasing the chances for inaccuracies coming from any patient movement. [4.] These are critical elements in SBRT because of the usage of high fraction doses and of small margins for planned target volume (PTV), thus requiring very high preciseness. Keeping in mind such benefits, in this thesis work, the commissioning of SBRT for 6 MV FFF photon beam was evaluated.

This thesis is organized in seven main chapters. The first one is the introduction, which gives a brief idea of what the thesis will be about. The second chapter describes the theoretical background relevant to the thesis work and the aim of this work. The third one is concentrated in the details of the materials and methods used to achieve such aims. The following chapter, fourth one, presents the results obtained during the work. The fifth chapter, discussion, covers the interpretation of the results obtained in the previous chapter. The sixth chapter gives a brief summary of the work and concludes in what extent the work aims presented earlier was achieved. The final chapter, references, lists all the references used throughout the thesis.

2. THEORETICAL BACKGROUND

2.1. Treatment of cancer

World Health Organization (WHO) defines *cancer* as the rapid creation of abnormal cells growing beyond their usual boundaries and affecting any part of the body as well as extending to other parts. Other terms referring to it in the medical society are malignant tumors and neoplasm. According to a study in 2008, cancer was found to be the leading cause of deaths worldwide with 7.6 million or 13 % of the total mortalities. The most common sites where cancer is found are lungs, prostate, stomach, liver, breast, cervix, etcetera; lungs being the most common one (1.37 million). By 2030, it is estimated that cancer deaths will increase to about 13.1 million. [5.]

Cancer can be reduced or controlled mainly by early detection and adequate treatment programs also known as cancer therapy. Cancer therapy aims to stop further progress of the tumour and its removal. The therapy includes four different methods which can be applied alone or in combination. These are: *surgery*, for the physical removal of the tumor mass; *chemotherapy*, a drug treatment for halting tumor's progress and reducing it; *immunotherapy* which uses body's immune system to change the immune response; and *radiotherapy* which uses the ionizing radiation for treatment. Radiotherapy or radiation oncology, which is in the scope of this work, has been a treatment option to various cancers for more than 60 years. [1.]

Radiotherapy, also known as radiation therapy, is the use of high energy X-rays to treat different tumors. Its aim is to diminish the tumor by delivering a high dose of radiation to the tumor site and expose as small as possible dose to the healthy tissues surrounding the target or to the ones in the beam's way. It is also used for palliative purposes rather than curing ones. It can be given from inside the body through sealed radioactive sources placed within the tumor volume, known as brachytherapy or from outside via external radiotherapy; the latter being in the focus of this thesis. External beam radiotherapy is the most common treatment method used in oncology. The radiation source is at a certain distance from the patient and uses an external beam to treat the tumor inside the patient. [1.] In most of the cases, this mode uses photon beam, however in less cases electron beams and even rarer proton or neutron beams (the last two are not yet well established in radiotherapy). The scope of this thesis covers only the photon beam and the other methods will not be discussed any further.

Photon beam is produced in two ways, gamma rays originating from radioactive nuclei and x-rays originating from the interaction of the accelerated electrons with the X-ray target installed in the machine's head. In the second case, the produced photons are due to the interaction of the accelerated electrons with the target atoms. Most of the kinetic energy is transferred into heat and a small part of it is used to produce the photon beam which consists of bremsstrahlung photons and characteristic ones. Based on the kinetic energy of the electrons, the photon beam can be produced either within an X-ray tube or in a linac. The photon beam produced from electrons with kinetic energy ranging from 10 to 100 keV are called superficial X-rays, the ones from 100 keV to 500 keV are called orthovoltage X-rays, and the ones produced with more than 1 MeV energy are classified as megavoltage X-rays. The first two groups are produced within the X-ray tube and the third one is generated by using linear accelerator. [6.]

A major element accompanying radiotherapy planning process is the imaging system which is most usually based on the computed tomography (CT). Diagnostic property of CT images is widely used in external beam radiotherapy for defining the target(s) and other structures relevant to the treatment. The images are geometrically accurate and provide electron density of the organs, needed for the dose calculations. However, its main pitfall is poor soft tissue contrast and it cannot accurately identify all the tissues and the target(s), due to different technical reasons. Therefore, other modality such as magnetic-resonance-imaging (MRI), which offers a very good soft tissue contrast, is used in combination (image fusion) with the CT to complement for the missing data. It should be in combination with CT because MRI cannot be used directly in the planning process due to the lack of electron density information. This is practically useful in the cases of head and neck, and brain tumors. Other modalities, used less frequently, are positron emission tomography (PET), single photon emission computed tomography (SPECT) and ultrasound. [1; 7.]

2.2. Medical Linear accelerator (linac)

2.2.1. Brief history of linac

Megavoltage external beam radiotherapy dates from 1937. It was the time when radiotherapy was in the transition process from being palliative to being a curative option for the tumor. The idea of linac was introduced as early as in 1928 from Ising, a Swedish physicist, who published "On a new principle for the production of higher voltages". However, due to the technological deprivation of that time, the implementation was possible only in 1953, when Metropolitan-Vickers Electrical Co Ltd (Mac-Vic) built the first linac in the world using 8 MV X-rays with the accelerating waveguide mounted vertically (4 m long) and with a stationary gantry.

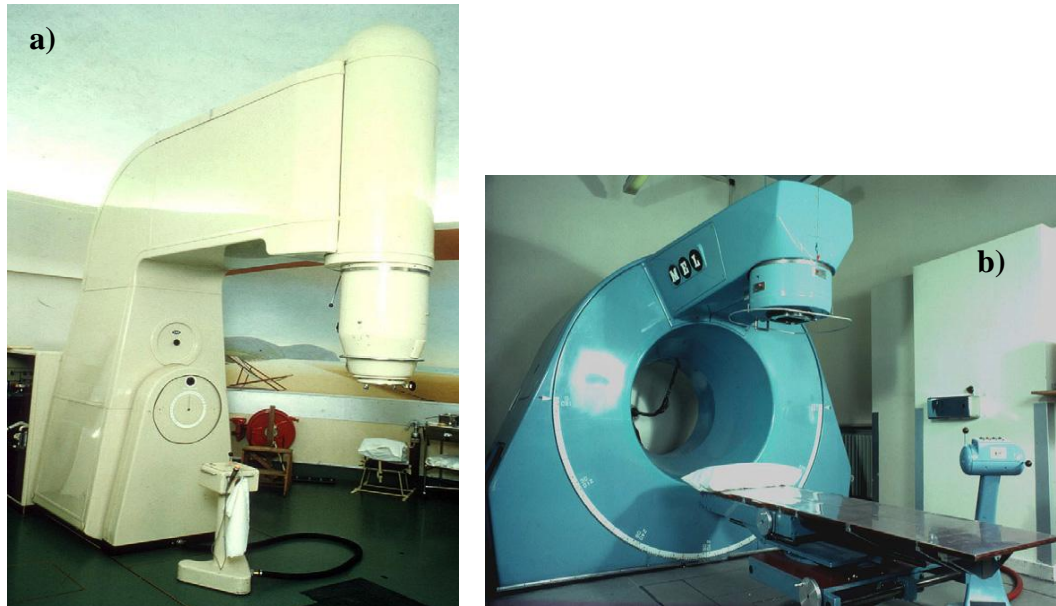


Figure 1. a) 4 MeV linac of 1950s from Mac-Vic, b) 6 MV linac, mid-1960s from Mullard Equipment (MEL). Adopted from [8].

Figure 1a shows a similar model (to 8 MV one) based on 4 MV photon beam, produced from Mac-Vic and figure 1b shows 6 MV linac of 1960's produced from Mullard Equipment (MEL). In 1962, Varian Company introduced the first isocentric 6 MV linac with a horizontal waveguide. As one can imagine, the machines had their own pitfalls and safety issues, mainly because it was new and not-well established technology. [8.]

Starting from the 1970s the linac had established itself; many more were produced which were also more stable and reliable compared to their predecessors. Since then, no other radical changes in the concept of clinical linac took place. Throughout the time the system was further enhanced and developed with additional and more advanced features leading to today's modern linacs. Due to different accidents, special attention has been paid in developing and improving the safety aspects in every step of the machine's operation. It is worth noticing that the technology has been neither stable nor user-friendly until 1980s-1990s when the major technological improvements (for example faster and more reliable computers) took place. Due to the rapid development of technology, today's machines, although use the same principle as the earlier ones, are far more advanced. They support various treatment modes, IMRT and VMAT with included X-ray tube together with megavoltage portal imaging device for imaging purposes. Due to these developments SBRT performance has significantly progressed. Needless to mention that safety of dose delivery and operation has progressed drastically. [8.]

The future of linac will be on the further consolidation and development of IMRT and especially of IGRT. An example of that would be the idea proposed in 2004 for the full integration of linac with MRI scanning machine [9]. Moreover, the possibility to combine external beam radiotherapy with other ones (for example chemotherapy) for better results is under investigation as well [1].

2.2.2. Modern linac

Clinical linacs are cyclic accelerators that accelerate electrons in a straight trajectory with kinetic energy from 4 to 25 MeV within a vacuum structure called accelerating waveguide. Today, different types of linacs exist, depending on the energy they use and their generated beam. Modern linacs are able to produce photon energies of 6 and 18 MV and electron energies ranging from 6 to 22 MeV and Varian TrueBeam STx (Varian Medical Systems, Palo Alto, CA) used in this paper is one of them.

The general structure of a medical linac is classified into five key components: treatment head (gantry), gantry support, modulator cabinet, patient support system and control console, with the most important one being the gantry. On the other hand, the beam is formed with the help of the following elements: injection system, radio frequency (RF) power generator, accelerating waveguide, auxiliary system, beam transport system, beam collimation and monitoring system (ionization chambers). Figure 2 shows a general schematic diagram of such linac. Depending on the producer, there are variations between machines according to the type of produced beam and its energy. [6.]

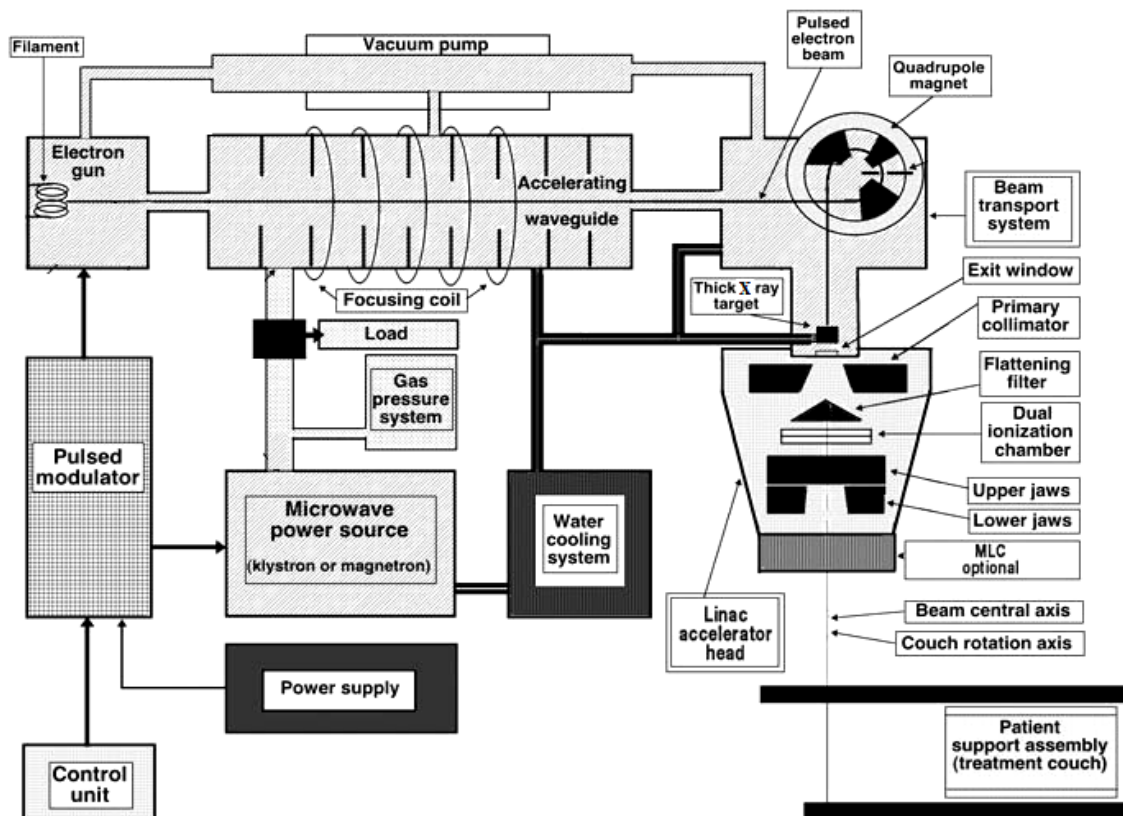


Figure 2. Main components composing medical linac. Adopted from [6].

Gantry mainly consists of retractable X-ray targets, flattening filters, primary and adjustable collimators, dual ionization chambers and multi leaf collimators (MLCs), as illustrated in figure 2. The target for photon beams is used in combination with the flattening filter which is mounted in a rotating carousel. *Beam collimation* is done via the

collimators, which are used for shaping the beam to the desired size. MLCs are optional in the linacs working with only three-dimensional radiotherapy (3DRT) but they are always present in the linacs that support IMRT modalities. They are used to shape the beam in the desired form and size. Usually there are 120 leafs, each of them accompanied with computer controlled motors. *Ionization chambers* are used for monitoring the photon beam output expressed in terms of monitor unit (MU). They are usually adjusted such that 100 MU corresponds to 1 Gy dose measured in water phantom, at the depth of dose at the central axis (CAX) for a field of $10 \times 10 \text{ cm}^2$ and source-to-surface distance (SSD)=100 cm. Other beam parameters controlled from this chamber are the beam's flatness, energy and symmetry. The two chambers work independently of each other so if one of them fails the other one still works until the treatment is completed. [10.]

RF power generator accelerates the electrons to the desired kinetic energy within the accelerating waveguide by using microwave radiation. It is referred as microwave power source in figure 2. *Injection system* is the component which produces the electrons and is called the electron gun. The basic injection system contains a filament cathode and punctured grounded anode. *Accelerating waveguide* is a vacuumed or gas filled metallic structure used for electron acceleration. Its length depends on the kinetic energy of the accelerated electrons and varies from 30 cm to 150 cm for kinetic energies varying from 4 MeV to 25 MeV, respectively. *Auxiliary system* consists of many factors which regulate the work of the linac, although not directly involved in electron acceleration. The key factors are water cooling system, shielding against leakage and vacuum pumping system. *Electron beam transport* transports the electrons from the accelerating waveguide to the X-ray target (high atomic number (Z) material), usually tungsten, or exit window via evacuated drift tubes and bending magnets. The bending angle depends on the structure of the machine and it can be of 90° , 270° or 112.5° . [6.]

Keeping in mind the major components of the linac just described here, one can easily understand the production of the clinical photon beam. In few words, the electrons are produced from the heated filament in the electron gun, serving as a cathode. These electrons are then transferred to the accelerating waveguide where they are accelerated to the desired kinetic energy. Next, the accelerated electrons are transferred to the beam transport system where the beam bending occurs. Through the bending process, the electron wave is directed toward the X-ray target which serves as anode. From the interaction of the two, the clinical photon beam, named also as X-rays, is produced (in the CAX direction). Most of the kinetic energy of the colliding electrons with the target is transferred into heat (the reason for the cooling system) and a small part of it serves for the photon production. From the interaction of the electrons with the target, two kinds of X-rays are produced: characteristic ones and bremsstrahlung ones. In brief, the first kind is generated as a result of Coulomb interaction between the incident electrons and the atomic orbital electrons of the target. Meanwhile the second kind is produced from the Coulomb interaction between the accelerated electrons and the nuclei of the target.

The ratio between these two types of X-rays is dependent on the kinetic energy of the electrons and of the target material. In the linac case, the bremsstrahlung X-rays dominate the produced beam. Until it reaches the patient, the beam goes through some processing. It is firstly shaped by the collimators, then flattened via the flattening filter and afterwards is shaped to the desired parameters via the jaw system and MLC system. [6.]

2.3. Clinical Radiotherapy

Since its implementation about 60 years ago, external radiotherapy treatment has gone through many developments [2]. There has been several treatment methods used during the time, depending on the technology of the day. However, here only the last few of them will be discussed: 3DCRT, IMRT, and VMAT which can be all used for SBRT treatments.

Today, radiotherapy treatment is already headed toward the intensity modulated beam treatment which is the common feature of the last two methods. Before explaining each of them, it will be useful to explain few clinical structure definitions.

2.3.1. Clinical structure definitions

The aim of radiotherapy is to irradiate the target meanwhile sparing the healthy tissues around the target as much as possible. Therefore, external photon beam is carried out by using multiple beams at different angles. An important factor of an efficient curative treatment is the volume definition of the involved structures within the patient's body. The main volumes defined from the radiation oncologist are the *gross tumor volume (GTV)*, *clinical target volume (CTV)*, *internal target volume (ITV)*, *planned target volume (PTV)* and *organ at risk (OAR)*.

GTV is the gross visible location of the tumor, including its extensions. GTV is practically defined by using any of the imaging modalities CT, MRI, ultrasound or a combination of any of them with each other. Other diagnostic modalities are also used.

CTV is determined by the oncologist and includes the GTV and other surrounding sub-clinical malignant diseases targeted for elimination. In most of the cases it is defined as the GTV with an additional margin (most typically between 0.5 mm and 1 cm) around it but in other cases it can be the same volume as GTV.

ITV is defined as the CTV with an additional internal margin. It predicts organ motion (for example breathing) leading to variations in CTV's location and size regarding to predefined reference points.

PTV is the volume that includes the ITV and usually an additional margin (for example of 1 cm) around it. This margin is added to account for geometrical uncertainties of treatment delivery, certain uncertainties of the machine and of the patient set-up, with the ultimate goal of total target irradiation. However, PTV does not take into consideration dosimetry uncertainties because that is taken care of from the treatment planning system (TPS).

Finally, OAR is defined as any organ that has a low radiation tolerance. In some cases, new field arrangements need to be done in the TPS so the OAR is not over-irradiated. OAR can be any organ that is in the beam's path, no matter the distance from the PTV. [6.]

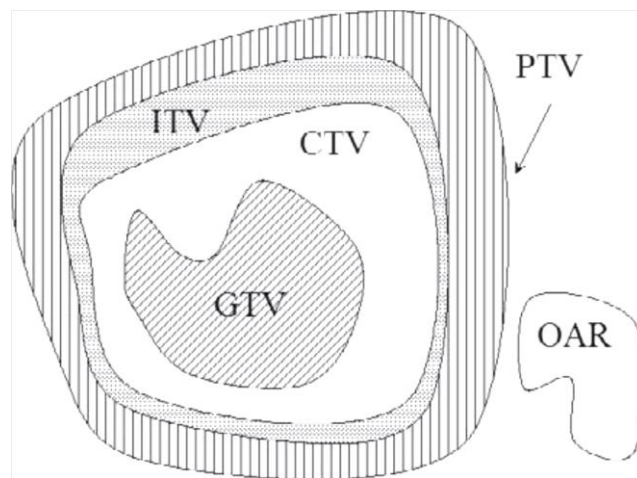


Figure 3. Schematic presentation of clinical structures. Adopted from [6].

In this thesis, PTV and GTV are utilized only, for two main reasons. Firstly, ITV and CTV are defined in clinical cases therefore they are not applicable to the simulations performed here and secondly, they are not common structures used in SBRT.

2.3.2. 3DCRT

In 3DCRT the treatment is based on 3D anatomical information and the treatment planning aims to have conformed dose distribution to the target and minimize the dose exposure of healthy tissues. The anatomical information is gathered by using two-dimensional (2D) image slices, which are then combined to create the 3D visualization. Afterwards, the delineation of the structures and targets is done through the *segmentation* process. Then, fields and beams necessary for the treatment are designed. The optimization problem in this case requires modifying constantly several parameters until the desired conformity is achieved. These parameters are the number of fields, their aperture, beam weights, their directions and beam modifiers (bolus, compensators, wedges). Multiple fields are used because it avoids the use of very high energy beams and spreads the dose in larger volume. However, creating more than four fields introduces the problem of the beam modifiers' production. [11.]

Beam shaping blocks were created for each field and were time and labor consuming not only in producing them, but also mounting and holding them during the treatment. This problem was significantly improved with the current development of MLC system which is used for beam shaping. To achieve the required optimization, beam parameters are selected based on trial-and-error method or experience and modified iteratively. This meant that for complicated cases, optimization could be a lengthy procedure, not to mention that it also depended on the planner's experience, speed of the calculating system and other factors. When the plan is optimized and the dose is calculated, plan evaluation is performed. The evaluation criteria include the dose distribution in the target and the dose delivered in healthy tissues. Isodose curves and surfaces can be displayed in any desired plan of the patient on the 3D anatomical image and are used to check the dose distribution. Dose-volume histograms (DVH) are used to control the dose delivered in each of the structures and target volumes. It gives information on the minimum, maximum, average dose distribution and its anatomical distribution. [11.]

2.3.3. IMRT

The idea of IMRT has started in 1970's but its practical implementation began later, in 1990's, due to the technological limitations. With the development of the more powerful computers and imaging techniques, the importance of IMRT has increased since. [1.] IMRT is based on the combination of two elements: inverse treatment planning accompanied with computerized optimization and the computer-control of the radiation intensity modulation carried out with MLCs during the treatment.

Inverse treatment planning

Inverse planning is one of the main advantages of IMRT over the conventional method. The key concept of it is that the person who makes the treatment planning chooses beam directions, target dose goals and the dose constraints for the structures surrounding the target volume. For example, the user defines the minimum and maximum dose to PTV and the maximum dose to the organs at risk. Based on the defined requirements, TPS performs the optimization process in which it divides the beam into smaller beams, called beamlets. Intensity of each beamlet is then modified to create the dose distribution which maximally fits the required one. If the final dose distribution does not meet the requirements, then the optimization process can be repeated by modifying goals and constraints of the treatment plan.

Technically speaking, goals and constraints are represented from the planning system as a cost function which should be maximized or minimized during the optimization process. The cost function is considered as a tradeoff between the goals and constraints based on the clinical judgement. Modifying any of the goals or constraints will change the cost function, thus the final result. The inverse planning and optimization process are considered to be very helpful and advantageous compared to the forward

planning. However, they do not always offer the best solution right away. That is why the cost function should best characterize the clinical concerns. In addition, the user should know how to regulate the cost function so the obtained result is better than the previous one. [13.] Figure 4 gives the comparison between the traditional (forward) planning with the inverse planning used in IMRT. The dashed lines show the dose target conformity which is better in inverse planning than in forward one.

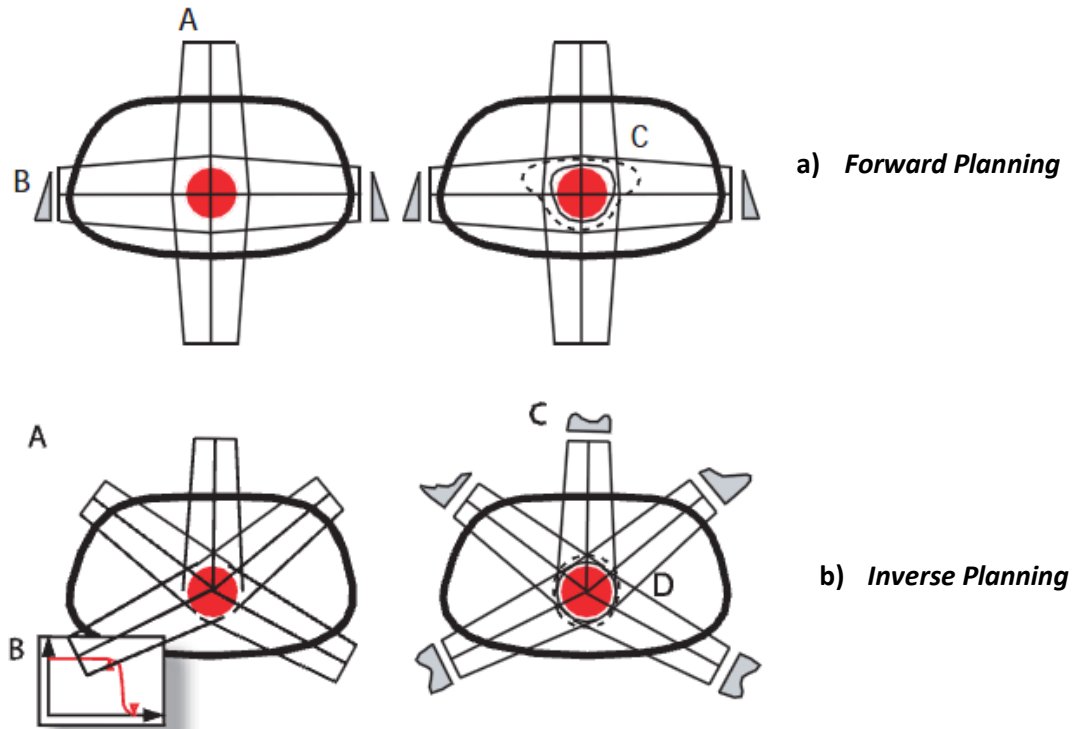


Figure 4. a) Traditional/forward planning. A: the setup of the fields conform the target volume (in red). B: beam modifiers to reach the required dose distribution. C: the final shape of dose distribution. b) Inverse planning: A: setup of field geometry. B: definition of goals and constraints for the desired dose. C: modulated fluence resulting from optimization. D: resulting dose shape distribution. Adopted from [12].

IMRT delivery

The beam modulation in IMRT is fully supported from the MLC system. MLC consists of opposing pairs of tungsten leaves which can be controlled independently. Its number depends from vendor to vendor. The use of MLC system means also that beam modifiers such as blocks and wedges are no longer used. [13.] Via MLC system variable radiation intensities are generated for each beam. This is done by dividing the beam into many beamlets, each with different intensity. The two most common delivery methods of IMRT are segmental MLC and dynamic MLC.

Segmental MLC

It has been derived from the conformal radiotherapy where for every beam several diverse MLC-shaped fields are produced. The beam is kept off during the field shaping and turned on when the shaping is completed. Next, the beam is turned off again, leafs move to the next position and then beam is turned on. This process is repeated until all the modulations are completed. That is why it is also called *step-and-shoot* technique.

Dynamic MLC

The only difference with the segmental MLC is that the beam is kept on during the field shaping. It is turned off only when the beam is changing the angle. The speed of leafs and distance between them is crucial in producing the desired radiation intensities. It was observed that it offers a better dose conformity when compared to segmental MLC. However, since the beam is all the time on, the dose leakage as well as total body radiation is higher. Dynamic MLC is known also as the *sliding window* technique. To summarize IMRT, table 1 gives some of the advantages and disadvantages of IMRT. [7.]

Table 1. Advantages and disadvantages of IMRT. Adopted from [7]

Advantages	Improved target conformity	Intentional dose inhomogeneity is possible	Better normal tissue sparing	Dose escalation	Can compensate for missing tissue
Disadvantages	Target and OARs outlining takes longer clinical time	Needs a broad quality assurance program	Machine treatment time is longer	Planning time is also longer	Scattered and leakage radiation is higher.

2.3.4. VMAT

Rotational arc therapy known also as VMAT or intensity modulated arc therapy (IMAT) has been proposed in 1995, even earlier than IMRT was implemented. The proposed idea was the same as it is today, the MLC modulated beams are delivered as the gantry rotates. However, its implementation took place few years later due to the technological inferiority of that time. VMAT (the term that will be used from now on) is similar to the IMRT with dynamic MLC. The difference here is that IMRT is applied in few certain angles, depending on the amount of treatment beams while VMAT is the IMRT application for every angle of the rotation arc around the patient. VMAT is considered to be a more efficient delivery method compared to IMRT and it is as good as or even superior to IMRT plans. However, its main drawback is the optimization process which is time consuming due to its demand for high computation power. In this aspect, multicriteria

optimization and the engagement of powerful computers have proven to reduce the optimizing time significantly. [14.]

In a recent study conducted for pulmonary SBRT patients with tumors nearby the chest wall, VMAT SBRT seemed to have some advantages compared to traditional SBRT treatments. The gantry movement at the same time as the MLC modulation offered more optimal treatment planning and dose delivery. Compared to IMRT SBRT method, it was noticed that in VMAT there was a considerable volume reduction in receiving the same prescribed dose. Table 2, which displays the average data gathered from ten patients included in the study, supports such advantage. [15.]

Table 2. A comparison of the volume of chest wall, rib volume and lung volume receiving the prescribed tumor dose of 30 Gy, for two different SBRT techniques. Data are the average for 10 patients included in the study. The significant difference between the volumes receiving the same dose shows the advantage of VMAT SBRT. Adopted from [15].

	Chest wall (cm ³)	Rib volume (cm ³)	Lung volume (cm ³)
IMRT SBRT	193.9	13	12.4
VMAT SBRT	47.6	6.3	10.2

Other advantage of VMAT SBRT compared to noncoplanar IMRT plans for lung treatments is the speed of treatment delivery. According to radiation therapy oncology group (RTOG) 0915, for the same treatment case, VMAT plan required an average time delivery of 6.5 min compared to 23.7 min for IMRT technique. It is a considerable difference because shorter delivery time leads to smaller risk for target motion and more comfortable treatment for the patient. [16.] Table 3 gives a good summary and comparison between non-SBRT and SBRT treatments.

Table 3. Comparisons between the non-SBRT and SBRT treatment methods. Adopted from [2].

Characteristics	3D/IMRT	SBRT
Dose fraction	1.8-3 Gy	6-30 Gy
Number of fractions	10-30	1-5
Target definition	May not have sharp boundary	Well defined, GTV=CTV
Margin	Centimetres	millimeters
Primary image modality used for treatment planning	CT	Multimodality: CT/MRI/PET-CT
Maintenance of high targeting accuracy during treatm.	Moderately enforced	Strictly enforced
Respiratory motion management	Moderate	Highest
Radiobiological knowledge	Moderately well understood	Poorly understood

2.3.5. SBRT

SBRT is a common technique used in radiotherapy for treating mainly early stage primary and oligometastatic cancers in thoracic cavities, abdomino-pelvic ones as well as in (para) spinal areas; the major treatment site being the lungs [2]. Stereotactic treatment started in 1992 in Sweden after an extracranial stereotactic frame was developed to be used for treating chest and abdomen tumors [9]. Since then, the technique has improved further and became more popular after seeing its advantages toward conventional treatments.

The key features characterizing it are the use of few fractions with very high doses used in small target volumes accompanied with small margins and utilizing a very precise localization of the target (optional is the use of patient fixation frames). Because of the high dose/fraction, the biological effects are also high both in non healthy and healthy tissues. To minimize the healthy tissue radiation and maximize the target radiation, a great priority is given to dose conformity. Not only is tumor localization very precise but also image guidance throughout the treatment is utilized. The precise tumor location is guaranteed by applying accurate structure delineation and advanced imaging techniques, MRI, 3D CT/four-dimensional (4D) CT, SPECT and PET. Moreover, compared to conventional treatments, in SBRT the number of treatment fields is higher. SBRT can be performed either with static fields (3DCRT), IMRT, a combination of the two or VMAT technique, depending on the treatment case. Also the beams can be coplanar or non coplanar, flattened or unflattened. [2.] The selection of these options becomes crucial when talking about dose delivery time. Often, long delivery times are problematic for patients who cannot stay in one fixed position due to the pains or medical problems they have. Thus, VMAT SBRT techniques are considered to offer the best solution. According to Holt et al. [18], SBRT using IMRT takes about 30 to 45 min as a total treatment time (including the patient setup and post-radiation monitoring), meanwhile VMAT SBRT takes no longer than 20 to 25 min for the overall treatment time. This advantage makes VMAT technique a more favourable option and that is one reason why it is the chosen one in this thesis.

In SBRT, the usual daily dose ranges from 8-30 Gy (conventional one ranges between 1.8-2.5 Gy) and the whole treatment course is expected to last one to two weeks. Application of such high dosage is seen to have better effects on the tumor, as it has been shown from different radiobiological reports. The complete response of the tumor after the SBRT was reported to be about 50 % and that is much better than the 20 % response coming from the conventional treatment. This implies that the tumor growth disrupts and becomes weak enough for the immune system to reduce it. However the dose delivery accuracy has to be very high so as less healthy tissue as possible is exposed to the high dose. That is why the treatment is conducted very carefully and the latest technology is applied to assess it. For more detailed information, RTOG 0236

protocol describes thoroughly the procedures to be followed for the application of SBRT technique and RTOG 0915 describes SBRT application for medically inoperable stage I peripheral non-small cell lung cancer (NSCLC). RTOG 0618 gives information on the non-small lung medically operable lung tumors using the same doses as in RTOG 0236 [17].

Patient selection criteria and recommendations

SBRT is mostly applied for medically inoperable patients (usually old aged) who suffer from other medical problems and long treatment times are an issue for them [18]. Patients with lung cancer chosen for SBRT treatments are squamous cell carcinoma, adenocarcinoma, large cell carcinoma, large cell neuroendocrine, and non-small cell carcinoma. The tumor is well defined and the maximum cross-sectional diameter reaches up to 5 cm. However, the diameter value varies from hospital to hospital and it can get also up to 7 cm in few cases. [2.] Another important aspect is the amount of beams applied in this treatment which however is not well defined because it depends on the hospital's experience and the case at hand. For example, the treatment of Stage I lung cancer has been treated with seven to ten non coplanar beams. According to RTOG 0618 recommendations, patients with operable stage I or II NSCLC are advised to be treated with non coplanar, non opposing beams. The recommended amount of beams is not less than ten, all with approximately equal weights. If static field SBRT is applied, not less than seven non opposing beams are advised. [3.]

Dose constraints

From this perspective, a common term used for parallel tissues (for example liver and lung) is the *critical volume*, which is defined as the absolute volume of an organ that must be saved in order for it to still function. For example, the critical volume of liver is one third, meaning that if more than that is removed or damaged, the organ will not perform its basic functions. For serial tissues (for example esophagus, nerves and airways) the damage is reliant on the maximum dose delivered and even a small damage of the organ may result fatal. Therefore, avoiding the serial tissue organs as much as possible and keeping in mind the critical volumes are some of the main priorities when applying SBRT. [17.]

Immobilization and motion assessment

As mentioned earlier, one of the crucial elements of the SBRT treatment is the patient fixation and motion evaluation. For this reason, various fixating equipments have been developed including body frames, vacuum pillows and frames used for local fixations. It is important that regardless of the chosen method, patient should feel comfortable during the treatment and the setup would be clinically efficient. The setup is recorded in detail in the patient's files, so it would be easy to reproduce the setup again

for the next treatment. Tumor motion is a delicate aspect to be dealt with, especially in SBRT when the treatment dose is very high and margins are very small. Most common cases of motion assessment are related to the respiratory ones. [17.] For the management of tumor movement various approaches are used, including tumor tracking, gating delivery and breath control techniques [16]. Motion assessment can be done also with different image modalities, depending on the case. For example, for lung tumors, real-time fluoroscopy and 4D CT can be used [17].

2.4. FF vs. FFF beams

The principle of a standard linac as explained earlier (in chapter 2.2.2) is to accelerate the electrons to kinetic energy from 4 to 25 MeV which hit the X-ray target to produce photon radiation. The flattening filter (FF) is located in the gantry of the linac, between the primary collimator and the ionization chamber (figure 1) and its purpose is to flatten the output dose so it has a uniform distribution at the reference depth. As shown in figure 1, it has a conical shape and is usually made of copper, but it can also be made of any other high Z material. Beside the beam uniformity, FF also causes the reduction of the dose rate and is a major reason for photons scattered from the head. [19.] The removal of FF from the path of X-ray beam would significantly increase the intensity of the beam, as the graph of figure 5 illustrates, and that has proven to be beneficial to external radiotherapy.

The development of new therapy techniques (for example stereotactic radiosurgery/radiotherapy (SRS)) and the better use of IMRT hinted that the inhomogeneous dose delivery is found to be more useful than it was considered before [19]. SBRT treatment has often been prolonged due to the limited dose rate and the necessity for using many beams, among others. The dose rate offered from conventional methods (adding here the setup time) has resulted in a total treatment time of about one hour for NSCLC treatment. This long time poses the risk of tumor displacement during the treatment and discomfort to the patient. That is why alternative methods such as flattening filter free (FFF) beam, which offer faster treatments through higher dose rates, are investigated. [4.] Brief advantages and disadvantages of FFF beams are given next.

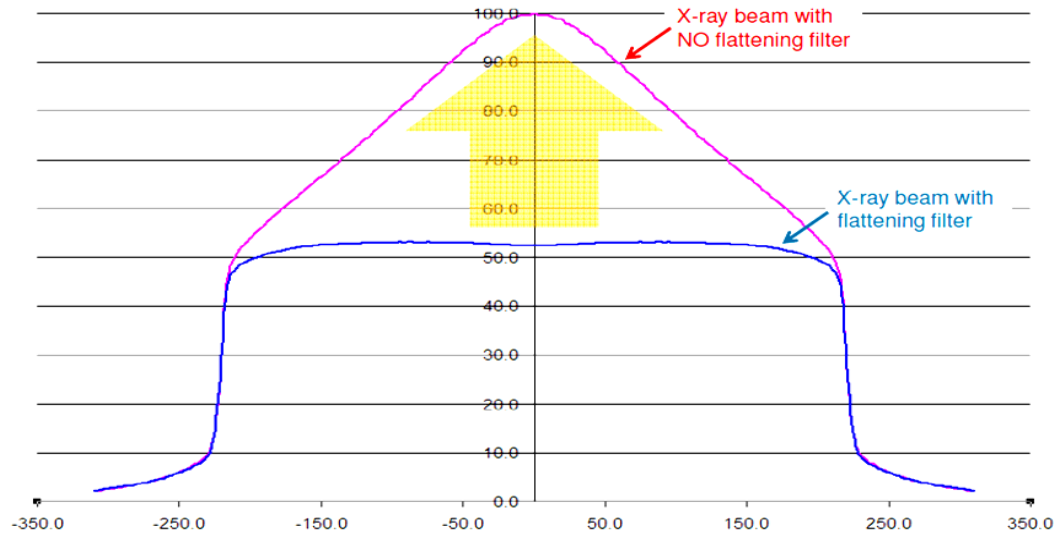


Figure 5. FFF X-ray normalized profile graphed against the flat (conventional) beam profile. X-axis gives the distance going further from CAX and Y-axis gives the dose in percentage. Flattened X-ray profile is generated by attenuating the raw beam with a flattening filter. FFF mode is achieved by removing the flattening filter from the X-ray beam path. Thus the intensity is increased (by nearly 200 %) near the central axis with an un-flat (conical shaped) beam profile, shown in pink. Adopted from [20].

2.4.1. Advantages of FFF beam

- Flattening filter removal increases the dose rate and dose per pulse, softens the beam and reduces the energy variation across the beam, the out of field dose and photon head leakage [19].
- The graph of figure 5 gives one of the main characteristics that distinguish the flattened beam profile and the FFF one. The increased dose rate leads to reduced treatment time compared to the FF beam, for the same amount of dose. For example, prostate and nasopharynx treatments were reduced on time by 43 % [21]. Also, the estimated delivery dose rate for FFF was 1400 MU/min which is between 2 to 4 times higher than the FF beam delivery dose [22]. Another experiment ran in Amsterdam University Medical Center gave evidence about the further advantages of the FFF beam in SBRT treatment. The study included twenty patients with ten of them having peripheral lung tumors and the other ten with vertebral metastases. VMAT was used to generate the treatment plans for unflattened 6 MV beams and the flattened one. Results showed that FFF beam plan's delivery time was 2.5 times shorter than the FF beam. [4.]
- Based on certain studies, it was noticed that the head scattering reduces to 1.5 %, compared to 8 % of the FF beam for the field sizes from 3x3 to 40x40 cm. The scattering reduction has a positive impact on lowering the risks of a secondary induced cancer for the treated patient. [4.] For these reasons FFF beam treatment seems to be beneficial for SBRT and SRS future treatments.

2.4.2. Limitations of FFF beam

Knowing that flattening filter free beam mode is a relatively new technology, there are still some uncertainties that need to be clarified before it becomes a full replacement to the flattened beam option. Some of the limitations presented from different published papers are reflected here.

- One aspect that needs to be dealt with is to set new technical criteria, standards and definitions regarding the FFF beam, similar as they exist for the conventional beam. Some of them include the initial acceptance measurements, and the periodic quality assurance which can be performed in daily, monthly or even yearly bases. [20.]
- The application of FFF beam requires further development of the today's MLC technology because for many optimized segments in static IMRT the traveling time of the leaf is too long and for dynamic and rotational IMRT, the speed of the leaf collimators is slower than required [19]. Moreover, the limitation is more evident for large treatment fields. When such fields are in use, MLC are used to regulate the central high intensity of the beam, for example supplying a more uniform dose within the large PTV. Consequently larger and faster MLCs are needed. Providing beam uniformity would also lead to a reduction in the initial dose rate, which actually was one of the main advantages of the FFF beam. [22.] This means that FFF beam delivery is more efficient in lesions of relatively small size [23].
- More information is needed when it comes to the immediate and long term biological effects of the very high dose rates on the healthy tissues and the ones inside the target volume [20]. In addition, all dosimetric properties and beam modeling, beam data acquisition and absolute dosimetry of the beam have to be carefully studied especially when it comes to small field applications [22].
- Lastly, some other uncertainties that need to be clarified are related to the higher dose rates and the performance of the radiation detectors, starting from the ion chambers to the portal imaging devices [24].

2.5. Treatment Planning System

2.5.1. Principles of radiotherapy treatment planning system

Generally speaking TPS is a system where the radiation treatment planning is done. The plan is based on the acquired images of the patient and the operator tries to optimize the dose distribution in the target volume as desired from the oncologist. Treatment planning systems have been developed a long time ago and the first ones were analog, dedicated to calculate the 2D dose distribution. The first such computer named “Wheatley Integrator” was reported in New York and was capable of working with irregular fields. The isodose distribution was represented with a matrix of numbers stored in punch cards. A similar method was used also in brachytherapy. Then, in 1960’s a digital computer (yet incomparable to the today’s ones) was developed to produce several depth dose tables and isodose charts. As technology started to develop even more, TPS developed into a more robust and user friendly tool. Every time technology advanced, TPS became faster and more accurate with better graphic displays.

As for the inverse planning, although it has been thought and studied since 1960’s, it became clinically useful only recently with the development of faster and more powerful computers. Today, TPS has improved sufficiently to plan in 3D, use images acquired from different imaging modalities, perform virtual simulation and provide DVH data. It also offers plan optimizations considering biological aspects and developed many other tools to make the treatment planning as accurate and user friendly as possible. [12.]

Eclipse TPS version 10.0 (Varian Medical Systems, Palo Alto, CA) provided from Varian is intended to support features that help in making an efficient treatment by providing beam modeling (treatment field(s) setup), patient modeling (by utilizing 3D imaging, characterization of the anatomical structures and target volume) and calculation algorithm. In addition, virtual simulation, dose calculation and plan evaluation is performed in order to support those functions. TPS consists of several important applications which are used in different stages of treatment planning construction.

Contouring application is used to prepare and modify the patient’s images according to the user’s requirements before the beam delivery is performed. Here the desired images can be selected, edited, deleted, imported, exported or modified. The application supports images coming from different imaging sources like CT or MRI. Images are 2D slices and their reconstruction forms the 3D model of the patient. Moreover, image processing is also provided here, mainly image enhancement (for example filtering). Relevant anatomical structures and targets can be outlined by using automatic or manual image segmentation. It is a crucial application because it is responsible for defining the anatomical structures relevant to the treatment; the better it is used, the more curative the treatment is. [1.] Another feature of Eclipse TPS is the image registration which is

an optional tool for the user. Image registration can be completed via automatic registration, manual translation, rotation and via registration points.

External Beam Planning is the application where treatment plans for target irradiation are constructed. It works based on the images prepared in the previous application and they are shown in three 2D different planes: frontal, sagittal and transversal as shown in figure 6; additionally it offers a fourth solid 3D image or beam's eye view (BEV) image, which is a 2D image reconstructed from beam direction illustrating patient's anatomy and beam modifiers. The purpose is to deliver the required dose to the target according to the user's specifications. The user can create and employ as many treatment fields as required and can characterize them individually. Field accessories can also be chosen here, including MLC, bolus, wedges and other beam modifiers. After the fields are planned, the dose calculation can be performed. Depending on the treatment method, optimization can be also performed prior to the dose calculation.

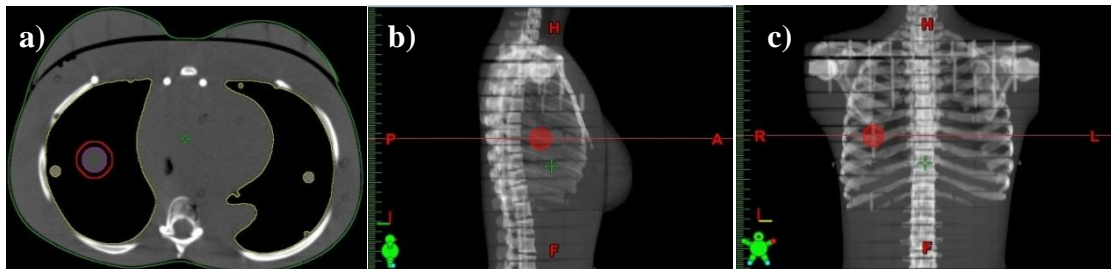


Figure 6. a) transversal, b) sagittal and c) frontal view of the PTV with diameter 3 cm in the central lung area. The red contour represents the PTV and the gray area inside PTV represents the GTV with diameter 2 cm.

Another important application in the Eclipse is the *plan evaluation*. As the name hints, it is used to analyze a plan or analyze and compare multiple plans in order to select the most appropriate one. When the dose calculation is completed, the dose distribution can be visualized in 2D either with isodose lines or color wash or in 3D by applying isodose surfaces or dose cloud modes. Beside the visual assessment, a numerical evaluation can also be employed by the use of DVH and dose statistics (max, min, average dose). Similar to external beam planning application, the current application also offers specific tools concerning the amount of MU used in each field, field weights, normalization options, dose at reference points and absolute dose. What makes the plan evaluation application special is the ability it offers to compare different plans side by side, add or subtract them even though they may be of different nature (for example brachytherapy plan and external beam plan). [12.]

2.5.2. Analytical Anisotropic Algorithm

A crucial element of the TPS is the dose calculation algorithm which is created to predict as accurately as possible the dose distribution within the patient. It is a very complex algorithm because of the complex interaction of the radiation beam with the patient's body. The algorithm is intended to consider the different tissue densities which

get in the beam's way and other parameters related to both the patient and the machine. Combining this complexity with the fast calculation demands presents limitations to the algorithm itself. Nevertheless, for common clinical conditions, it delivers very good results for reasonable time duration. Important to mention is that the accuracy of the algorithm at some extent depends on the user's input. Before it does any calculation, every algorithm needs some input data which is used as reference points for the dose computations. Therefore, the accuracy depends on the scale of the uncertainties of the physical measurements, the type and size of the used detectors and many other factors. The main difference between different TPSs is the dose calculation algorithm that each of them uses and for commercial reasons, these algorithms remain disclosed. [25.] The one used in Eclipse TPS is called analytical anisotropic algorithm (AAA) version 10.0.28 (Varian Medical Systems, Palo Alto, CA).

AAA algorithm used in Eclipse treatment planning system is a fast and accurate algorithm that calculates the dose in both homogeneous and non homogeneous tissues for all types of photon external beam treatments. The algorithm is based on a 3D pencil beam convolution-superposition algorithm which models the primary photons, scattered extra-focal photons and electron scattering independently. The analytical convolution employed by the algorithm reduces the calculation time considerably. AAA algorithm configuration is mainly based on Monte-Carlo stimulations and beam modifiers (for example MLCs, wedges, compensators and others) are included in the final dose calculations. AAA algorithm is composed of two main elements, *configuration algorithm* and *actual dose calculation algorithm*. [26.]

Configuration Algorithm

This module approximates the phase space of the linac's photon beam which contains information about the particle type of the beam, fluence and energy. The approximation is done with the help of a multiple source model consisting of the primary photon source, extra focal photon source (second source) and the electron contamination model source which are shortly explained next. The aim of this module is to process the measured data of the beam and verify them for any measurement imprecision; if positive, they are corrected. [27.]

The primary photon source represents the photon spectra which describes the interaction of the accelerated electrons with the X-ray target producing the bremsstrahlung photons. The spectra are modeled from the Monte Carlo methods and are tested for various targets within the Varian linacs. Another task of this source is to model the beam hardening effect from the flattening filter which tells that the photon's beam mean energy declines as the distance from CAX increases. [27.]

Extra focal photon source, also known as the second source, models the photon produced outside the target, within the accelerator's head. The effect of secondary photons is higher outside the beam defined from the primary source than inside. This is explained from the fact that the secondary source lies lower than the primary one thus the deviation is higher. However, this effect does not exist in the FFF beams because the flattening filter is the main source of deviation and removing it eliminates the problem.[26.]

Electron contamination source models the dose in the buildup region not taken into account from the primary and secondary sources. Its second function is to describe the photons coming from electron interactions, classified as contamination. In the photon beam, the contamination depends significantly on beam energy and field size. Electron contamination in the primary photon beam results from the flattening filter, collimator jaws and air, when no beam modifiers are used. In case modifiers are used, they become secondary electron contamination sources. Electron contamination is given by a depth-dependent curve which shows electron contamination dose versus depth. [26.]

Photon dose calculation module

For the volumetric dose distribution calculation, the body is modelled as a grid of individual voxels where the voxel size is determined from the selected grid size (minimum 1 mm). The geometry of the voxel matrix is aligned with the fan beam lines and based on the patient's CT images, electron density is calculated for every voxel [27]. The beam is split into beamlets which are along with the body's voxels. For each beamlet, dose calculation module calculates the dose. The superposition of the individual doses results into the final dose calculation. All AAA measurements and calculations are done in a water equivalent medium and then adjusted to the tissue density of the patient. [26.]

Photon dose calculation is done by considering the photon beam attenuation and photon scattering for each beamlet. It is expressed as the energy deposition density function $I_\beta(z, \rho)$ and considers also the tissue heterogeneity; photon scattering is expressed as a scatter kernel $K_\beta(x, y, z)$. First, the dose convolution is calculated in terms of energy and then by using the scaled-water estimation, it is converted into dose. The energy at a certain beamlet is calculated by using equation 1.

$$E_{ph,\beta}(\tilde{x}, \tilde{y}, \tilde{z}) = \phi_\beta * I_\beta(z, \rho) * K_\beta(x, y, z) \quad (1)$$

where $E_{ph,\beta}$ stands for the photon energy at beamlet β . While $(\tilde{x}, \tilde{y}, \tilde{z})$ gives the relative position of (x, y, z) with regard to the origin of the beamlet coordinate system. Symbol ϕ_β is the homogeneous photon flux in the beamlet's cross-section. In more details, $I_\beta(z, \rho)$ is given in equation 2 where z is the depth of the energy deposition, ρ is the

electron density and z' is used instead of z in order to consider the non homogeneities between the calculation point and the entry point of the beam.

$$I_{\beta}(z, \rho) = I_{\beta}(z') * \frac{\rho(0,0,z)}{\rho_{water}} \quad (2)$$

Tissue heterogeneity is accounted by utilizing the radiological depth Z' given in equation 3:

$$Z' = \int_0^Z \frac{\rho(0,0,t)}{\rho_{water}} dt \quad (3)$$

A similar method followed for the beamlet's photon dose calculation is used to calculate the primary and secondary photon sources. However, spectral composition, focal spot size and position are excluded from the calculations.

Superposition and dose conversion

The total absorbed energy at any voxel in the patient, expressed as $E(\tilde{x}, \tilde{y}, \tilde{z})$, is calculated by adding the individual energies coming from primary photon source, secondary photon source and electron contamination source for each beamlet, β , which are represented respectively by the first, second and third elements within the parantheses of the right side of equation4.

$$E(\tilde{x}, \tilde{y}, \tilde{z}) = \sum_{\beta} \left(E_{ph1,\beta}(\tilde{x}, \tilde{y}, \tilde{z}) + E_{ph2,\beta}(\tilde{x}, \tilde{y}, \tilde{z}) + E_{cont,\beta}(\tilde{x}, \tilde{y}, \tilde{z}) \right) \quad (4)$$

Finally, to obtain the dose, the total energy calculated from equation 4 is converted into dose by assuming that different non homogeneities can be modelled as scaled water. The dose resulting from this conversion is given in equation 5.

$$D(\tilde{x}, \tilde{y}, \tilde{z}) = cE(\tilde{x}, \tilde{y}, \tilde{z}) * \frac{\rho_{water}}{\rho(\tilde{x},\tilde{y},\tilde{z})} \quad (5)$$

Coefficient c is used for the unit conversion from J/m^3 to Gy.

Monitor Unit calculation

In radiotherapy it is very important to check the correct delivery of the radiation to the patient before and during the treatment. One of the main components of this control is the estimation of the MU. MUs are estimated independently and provide information on the amount of radiation delivered to the patient or the linac's output. Back in time it used to be manually calculated and to be sure, two independent persons did the calculations. Because the used methods were almost the same, the agreement between the results was not difficult. However, the development of advanced computers, 3D imaging and modern TPSs has changed the way MUs are calculated. Today's algorithm applied

for the MU calculation are based on 3D patient modeling and non homogeneous tissue density, thus making it more accurate, very complex and making the manual calculation almost impossible. [28.] Monitor unit calculation depends on many factors. The contribution of prescribed dose, field weight, plan as well as field normalization and the normalization factor itself are considered when calculating the final MU. For AAA, the normalization factor is the value of MU equivalent to 1 Gy to 100 % of the current field. Therefore, the MU expressed as MU_{norm} is calculated at the normalized point from equation 6.

$$MU_{norm} = CBSF(x, y) * \left(\frac{MU_{calib}}{D_{calib}}\right) * \left(\frac{D_{ref}}{D_{norm}(x,y)}\right) * \frac{1}{WCF(x,y)} \quad (6)$$

Where $CBSF(x, y)$ is the collimator backscatter factor for an open field. It is calculated by using the output factor results obtained during the beam data configuration.

MU_{calib} is the value of reference dose in MU at calibration depth. It is given from the user.

D_{calib} is the value of reference dose [Gy] at calibration depth, also given from the user.

D_{ref} is the calculated dose from AAA at the calibration depth for the reference conditions. It is considered also as the absolute dose scaling factor value.

$D_{norm}(x, y)$ is the dose calculated at the field normalization point.

$WCF(x, y)$ is wedge correction factor with the collimator jaw settings. In this thesis, no wedges are used, therefore its value = 1.

For more detailed information on the calculation techniques used from AAA, one can refer to the Eclipse Algorithms Reference Guide provided from Varian Medical Systems [26].

2.5.3. Optimization of dose distribution

Before the calculations are completed the plans need to be optimized in order to meet the dose-volume objectives. For this reason, four optimization algorithms are used from the AAA algorithm: dose volume optimizer (DVO), plan geometry optimization algorithm (PGO), progressive resolution optimizer (PRO) and multi-resolution dose calculation (MRDC).

DVO, used for IMRT treatments, optimizes the field shape and intensity by changing continuously the dose distribution within the target. Since it works based on iterative method, the initial (fluence) guess is zero. Then, the fluence is iteratively optimized from the algorithm and the dose of the new fluence is calculated.

PGO is supported from the DVO algorithm and it utilizes the same objectives. Its aim is to automatically choose the optimal beam angles which help to speed up the achievement of defined dose-volume goals set from the user. Although they use the same DVH-based objectives, PGO runs before the DVO.

PRO creates the VMAT (named by Varian as RapidArc ®) plans according to the dose-volume requirements and other objectives presented from the user. RapidArc mode uses dynamic MLCs (DMLC) with their position and MU/degree defined with respect to the gantry angle. Moreover, to reach the predefined dose-volume objectives, the dose rate and gantry rotation speed are changed during the dose delivery.

Dose modelling is done by dividing the field into equal small segments and for each of them the dose calculation is performed. In the dose calculation there are several parameters taken into account, the dose fluence of the apertures, leaf motion and angle resolution. Before the optimization process starts, the collimator leafs are conformed to the target and dose rates are the same for each segment of the field. At the start of the process, the larger adjustments are done to leaf sequencing and as the process continues, the adjustments get smaller. As the optimization continues, the dose calculation accuracy and dose distribution improve. Finally, the PRO algorithm during the optimization also takes into account the non homogeneity correction and air cavity correction factors.

Dose-Volume objectives

The objectives for the desired dose-volume are given in two kinds, upper objective and lower objective. Upper objective gives the maximum radiation allowed to be given to a defined volume of a structure. Lower objective determines the minimum desired dose to be given to a certain volume of the chosen structure. In both cases, the desired dose and respective volumes are given from the user.

Normal Tissue Objective (NTO)

It is used to prevent the hotspots (very high dose regions) in the healthy tissues outside the PTV and apply a sharp dose gradient outside the PTV. This parameter is defined from four different factors, the distance from the PTV border (x_{start}), start dose (f_0), end dose (f_∞) and fall-off factor (k). The first factor, (x_{start}), defines the area where NTO value is constant, expressed in cm. The second and third factor, (f_0) and (f_∞), decide the relative dose in % of the NTO at the PTV border and furthest from the PTV border, respectively. Lastly, the fall-off factor defines the sharpness of the NTO curve. The function of the NTO is computed from equation 7.

$$f(x) = \begin{cases} f_0 e^{-k(x-x_{start})} + f_\infty (1 - e^{-k(x-x_{start})}), & x \geq x_{start} \\ f_0, & x < x_{start} \end{cases} \quad (7)$$

To control the significance of NTO compared to other objectives, the *priority* factor is used. The higher this factor, the higher the importance of the optimization objective; value 0 means that the objective is not taken into consideration from the optimization process. [2.]

2.6. Aims of the thesis

The purpose of this thesis is to achieve the commissioning of the 6 MV FFF photon beam for SBRT lung treatments. This is done by comparing the TPS-calculated dose distributions with the measured ones for two different target volumes for four different fraction sizes. SBRT was delivered using VMAT technique. The comparison is done with gamma analysis and consulting technical reports series (TRS) 398 protocol.

3. MATERIALS AND METHODS

All the calculations and measurements were performed at the department of radiotherapy at Tampere University Hospital (TAYS). Prior to any calculation, the phantom was scanned using Toshiba Aquilion LB X-ray CT (Toshiba Medical Systems Corporation, Tokyo, Japan) machine at 120 kVp using slice thicknesses of 3 mm and field of view 52x52 cm (reconstructed image). The phantom used for the calculations was Alderson female ART phantom. It was constructed in horizontal slices of 2.5 cm thickness. Within the phantom there were materials that had equivalent densities to the bone, soft and lung tissues, respectively. Lungs, which were the focus of this work, were constructed with syntactic foam with specific gravity of 0.3 g/cc. After the scanning, images were electronically transferred using digital imaging and communications in medicine (DICOM) standard and saved in the treatment planning system software.

3.1. Target contouring

On the acquired CT images two separate spherical GTVs with diameter 2 and 5 cm and with electron density values equal to zero Hounsfield unit (HU) were created. HU values were calibrated to electron density using RMI-phantom (Gammex, Middleton, WI). Usually, from the department's experience, the range of HU values for GTV was between -30 to 30 HU, therefore the average was picked. Using the margins of 0.5 cm for GTV, two PTVs with diameter 3 cm and 6 cm were created in the central right lung area as illustrated in figure 6 and 7, correspondingly. These values were chosen as such because these are the typical minimum and maximum target volume sizes in the department. From now on PTV of diameter 3 cm and PTV of diameter 6 cm will be referred to as PTV 3 and PTV 6, accordingly. For a better comparison, all the created structures were isocentric. Then, segmentation process of the structures was implemented with the segmented organs being the lungs and the body (figure 6 and 7).

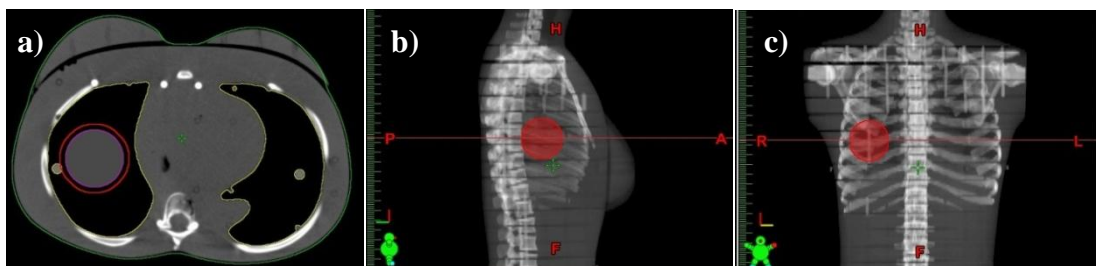


Figure 7. a) transversal, b) sagittal and c) frontal view of the PTV with diameter 6 cm (PTV 6) in the central lung area. The red contour represents the PTV and the gray area within the PTV represents the GTV with diameter 5 cm.

3.2. Dose planning

As soon as the targets were created and structures were delineated, the calculation process in the TPS was started. Eight VMAT plans (with the isocenter at the center of PTV) were generated in Eclipse TPS. The machine was set to operate on SRS VMAT mode, using a single beam for the RapidArc technique consisting of 1 coplanar partial arc with control point (CP) spacing of two degrees. When choosing the direction of the SBRT beam, one should take into account several parameters such as machine limitations, shorter beam path and most importantly avoiding the organs at risk as much as possible. The direction factor becomes less important when multiple directions are used [2]. Therefore, to have a more realistic situation, the chosen direction of the beam was from the right side of the lung only, so the left lung is spared from unnecessary dosage. In all cases the arc started at 181 degrees and terminated at 45 degrees in the clockwise direction; to avoid the MLC tongue-and-groove effects the collimator was set at 30 degrees and the collimator jaw tracking was activated. Figure 8 gives a general illustration of the beam setup in 3 different planes, together with 3D reconstructed image. This was applied for every plan. To better control the dose conformity in the target, the field size was controlled by using the BEV graphics. Maximum field size used in each plan is shown in table 4.

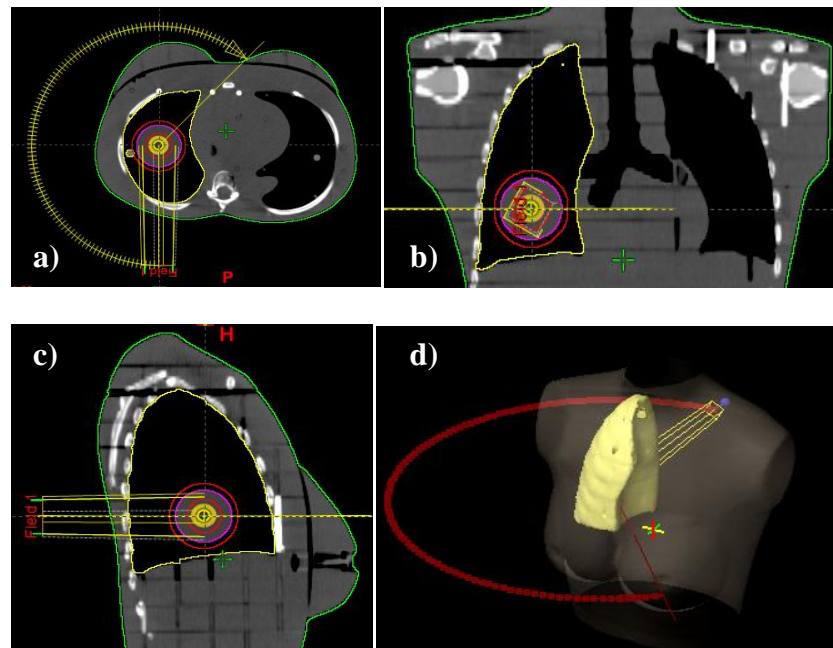


Figure 8. Beam setup (the yellow arc) viewed from different planes: a) transversal, b) frontal, and c) sagittal. The red contour represents the PTV and gray area represents the GTV. d) 3D modeling where the arc of the beam delivery is shown in red.

Table 4. Maximum field size for different PTVs and fraction sizes.

PTV d(cm)_dose fraction (Gy)	3_4	3_7.5	3_11	3_18	6_4	6_7.5	6_11	6_18
Field size X*Y (cm ²)	4x3.8	3.2x3.3	4x4.5	4x4.5	7x7.5	7x7.5	7x7.5	7x7.5

Isocenter of the plans was located at PTV's center point. The selected dose rate was the nominal one, 1400 MU/min. In general, the dose/fraction used clinically for SBRT treatments depends on the stage and location of the tumor. In this work, the applied fractionation scheme for each PTV was 8x7.5 Gy, 5x11 Gy and 3x18 Gy. These values are also the most typical ones used in the department and also have been used in other centres [4; 29; 30]. In addition to these values, more conventional fractionation of 15x4 Gy was added in the study. Because it is a small dose/fraction, it cannot be considered for SBRT treatment. However, this addition was done for study purposes only.

3.3. Optimization of dose distribution

After the beam setup, for each plan, the individual optimization of dose distribution for each dose level followed. VMAT optimization options such as the upper objectives, lower objectives and priorities were selected keeping in mind the RTOG 0915 protocol. This protocol which is widely consulted for SBRT treatments, suggested that several criteria have to be met for the clinical dose calculation to be acceptable. The criteria used in this thesis concern mainly the dose conformity evaluation. The ones concerning the organs at risk are neglected because they are irrelevant to the scope of the work. Therefore, the standards used here are: 95 % of the target volume (PTV) receives 100 % of the prescribed dose and 99 % of the volume receives at least 90 % of the prescribed dose. The volume of the 105 % of the prescribed dose outside the PTV should not be more than 15 % of the PTV volume [16] and the maximum dose inside the PTV should be between 110 % and 140 % of the prescribed dose [30]. These were the initial values plugged in the optimization window; however, to achieve a better dose conformity, they were slightly adjusted and some iterations were performed.

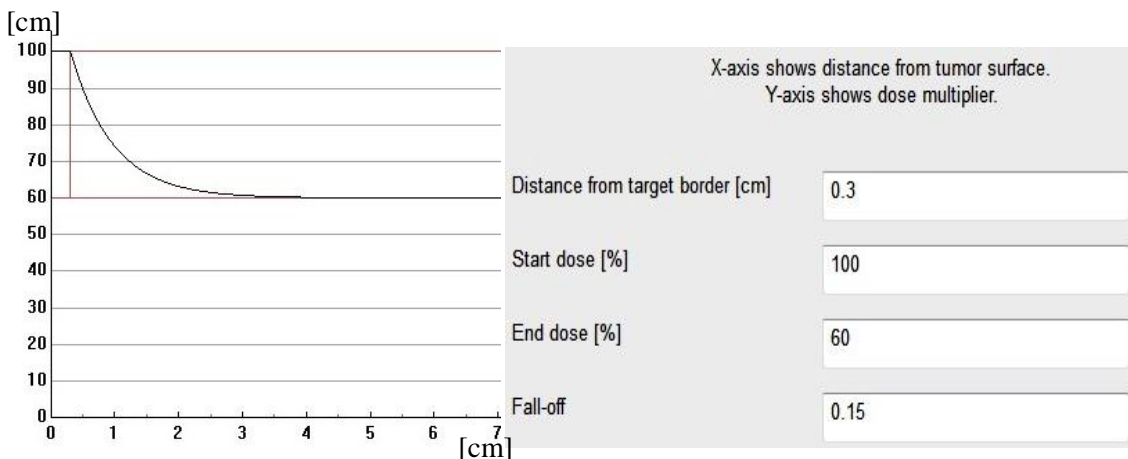


Figure 9. Normal Tissue Objective parameters chosen during the dose distribution calculation. a) graphic representation, b) selected parameters.

Optimization process computes the optimal fluence maps which is then converted into the actual fluence maps via the MLC system. To get a sharp fall-off dose outside the target volume, NTO parameters were selected as shown in figure 9 and the priority

for “normalization tissue” was set to be high. The X and Y jaws were kept dynamic, thus their aperture depended on the field size and MLC motion.

After all parameters were defined, calculations for the optimized plans were generated using AAA algorithm with grid size 0.25 cm and with tissue heterogeneity consideration. The use of grid sizes greater than 3 mm is discouraged for SBRT [30]. In this process, several data were calculated, including here the amount of MU used for each field, the dose received from the target, lungs and body, respectively. Dose normalization was chosen such that 95 % of the target receives 100 % of the prescribed dose.

3.4. Plan evaluation and verification

After the computations were completed, the plan evaluation was performed both visually and numerically. In TPS visual evaluation was done by checking the dose conformity within the target and the location of the hotspots. As for the numerical evaluation, isodose levels were accounted as well as dose statistics such as minimum, maximum and mean dose for each PTV.

A very common method to check the dose distribution in every structure is the DVH. It displays the dose distribution uniformity with regard to the structures' volumes in a 2D graph. In one single line it gives a very good evaluation of dose distributions for every structure involved in the dose calculation. It does that for one or more plans at once. For external beam radiotherapy, there are two types of DVH: cumulative and differential. Cumulative DVH shows the relative (in %) or absolute (in cm^3) volume of the structure receiving a predefined dose. The structure volume in % or cm^3 is given in the Y-axis and the X-axis represents the amount of dose either in % or in Gy. On the other hand, the differential DVH illustrates the share of the accumulative volume in structures receiving a particular dose with regard to equivalent dose intervals. In this thesis, the cumulative DVH is used. Sharper the curve drops down, the better is the dose uniformity [11].

Plan verification was the next step taken. Verification plans are created with the aim of verifying the accuracy of the treatment plan prior to patient treatment. It contained the same beam size, beam energy and angle as in the original patient plan, including here also the amount of used MU, field accessories, fluencies and MLC motions. In addition, the phantom was located at the isocenter exactly as the planned patient. For each of the treatment plans, the verification plans were created using the solid water phantom which CT images were priorly taken.

3.5. Dosimetric Verifications

The verification plans were transferred to the Varian TrueBeam STx linac machine which was calibrated to deliver 100 MU per 1 Gy for a field size of $10 \times 10 \text{ cm}^2$ and SSD=100 cm at depth of maximum dose. The MLC system contained 120 high definition leafs (HD-MLC) with leaf width of 2.5 mm (32 of them per bank) and 5 mm (28 of them per bank), leaf transmission less than 2 %, minimum dynamic leaf gap of 0.25 mm and maximum leaf speed of 2.5 cm. Dose rates supported for FFF beam were 1400 and 2400 MU/min for 6 MV and 10 MV, respectively. During the dose delivery, based on the data coming from TPS, linac coordinates three parameters: gantry speed, dose rate and MLC speed. Then the dose is delivered through the CP within the arc segment and between these points interpolation was performed. Because of the high complexity of the delivery, verifications of the dose distribution (usually in 2D) are always required.

There are several options used to measure 2D dose distributions: films, ionization chambers, ionization chamber arrays, electronic portal imaging devices (EPID), radiographic and radiochromic films [31]. Each of them has their own advantages and limitations. For example, EPID offers very good resolution and real-time analysis but it could not be used in the current measurements because there is no proper model of it for FFF beams, yet. For the current study, the verification and accuracy of the delivery, compared to the calculations was made using two different types of dosimetry: ionization chamber matrix detector (combined with cubic solid water phantom and mounted in the gantry) and radiochromic films. In each case, the calculated dose maps were exported to the OmniPro Im'RT software version 1.7 (IBA Dosimetry, Schwarzenbruck, Germany). To be able to compare measured (both from detector and radiochromic film) and calculated data with each other, the grid size of each of them had to be converted into a common spatial resolution. The grid conversion based on linear interpolation was done from 0.7619 cm to 0.1 cm for measured data and from 0.047 cm to 0.1 cm for calculated data.

3.5.1. Matrix detector on treatment couch

In the first scenario, shown in figure 10, the Im'RT ion chamber matrix detector (IBA Dosimetry, Schwarzenbruck, Germany), commercially named as MatriXX^{Evolution} (which from now on will be referred to as MXX) is used. MXX is a 2D digital verification system supported from the OmniPro Im'RT software. It is used for the verification of 2D dose distribution and usual for the quality assurance (QA) of high energy photon and electron beams, before the treatment. It is composed of 1020 ionization chambers with individual volumes of 0.08 cm^3 . Chambers were organized in a 32×32 matrix with gap between them equal to 0.7619 cm. The chambers are ionized when the photon beam goes through them and with the help of an electrical field the released charge is divided between the upper and lower electrodes. The current in the chambers is proportional to the dose rate falling into the matrix. The current is estimated and converted into a digital

signal thus giving information on the dose rate in each chamber. Further technical details are given in table 5.

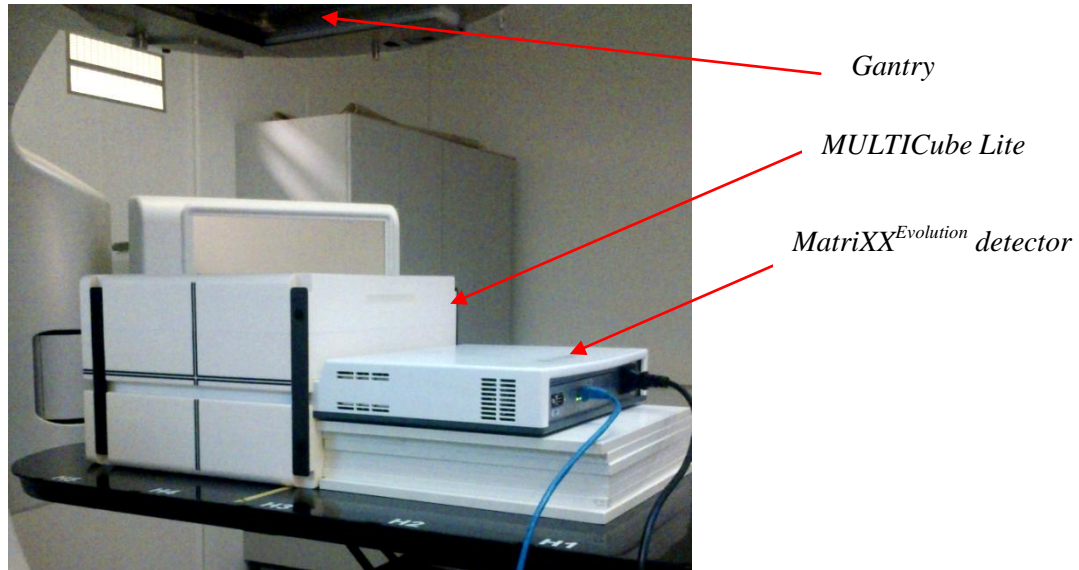


Figure 10. MCube-MXX setup on the treatment couch. Detector is sandwiched between the MCube phantom, on the treatment couch. The gantry irradiates the phantom while rotating, as planned.

MXX was then inserted into a solid water phantom, called MULTICube Lite (IBA Dosimetry, Schwarzenbruck, Germany). Its size was 31.4 cm in length by 34 cm in width by 21 cm in height. It is made of polystyrene with mass density of 1.04 g/cm^3 with 11 cm above and 10 cm under the matrix detector. Solid water plates seen in the image were used only to support the electronic part of the detector and had nothing to do with the measurements. MXX was calibrated for FFF beam and open field of $10 \times 10 \text{ cm}^2$ and before the measurement, the matrix was warmed up for 15 minutes, as recommended from the manufacturer [32].

Table 5. Technical data on the MatriXX^{Evolution} used for the measurements.

Item	Characteristics
Sensor type	Vented parallel ion chamber
Number of sensors	1020, arranged in a 32x32 grid
Active measurement area	24,4x24,4 cm
Chamber diameter	4.5 mm
Chamber height	5 mm
Chamber volume	0.08 cm^3
Distance between chambers	7.619 mm
Minimum dose rate	0.02 Gy/min
Maximum dose rate	20 Gy/min
Water equivalent depth	3.2 mm

The gantry and collimator angles of the linac were set to 0 degrees and the matrix was positioned on the treatment table in the centre of the beam with the guidance of light field. Then, MXX was connected with the computer in the control room through an Ethernet cable. Distance between the effective point of the MXX and the beam source was kept at 100 cm.

Due to the complex construction of the matrix detector, the sensitivity of the pixels is slightly affected from the beam coming at different angles during the gantry rotation and this dependency may influence the measured results. Therefore, a gantry angle sensor was attached to the gantry for angle estimation. Its purpose was to correct the measurements for angular dependence during the gantry rotation with the correction factors provided by the vendor. Finally, irradiation was performed as in patient actual treatments with gantry rotating around the phantom.

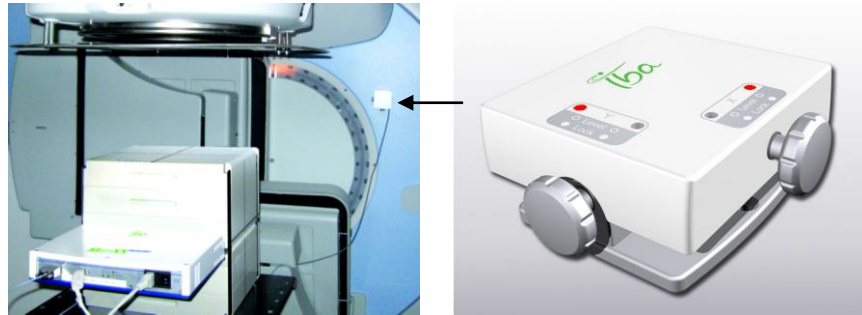


Figure 11. Angle sensor mounted on the gantry and connected with the detector. Adopted from [33]

3.5.2. Matrix detector mounted on treatment head

In this case, the MXX is mounted on the treatment head via a dedicated frame. Different from the previous case the gantry angle sensor was not used. This is because the gantry and the detector were attached to each other such that the beam was perpendicular to the detector during the whole irradiation and there was no change in the angle between them.

Moreover, plates which are water-like polystyrene were put between the detector and the frame, for a total thickness of 5 cm above the matrix. The isocenter was located on the surface of the matrix. Before the measurements took place, MXX was also calibrated for the FFF 6 MV beam of field size 10x10 cm. Figure 12 shows the setup of the measurement.

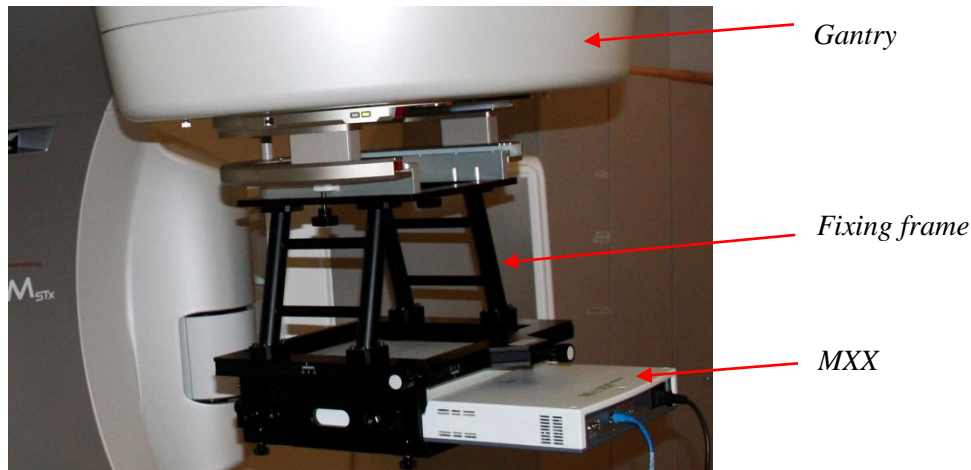


Figure 12. MXX mounted on the gantry with the help of the dedicated frame.

3.5.3. Film measurement

Results of many electronic detectors for dose distribution verifications have been widely published. For example, a brief, precise summary of them is given from Poppe et al. [34] and as it has been reported, due to the high spatial resolution, film measurement is the standard and the most accurate method for 2D dose distribution verifications. Its major disadvantage is the film procedures being very time and material consuming. Moreover, these procedures (for example calibration, scanning, and irradiation) require very high accuracy and stable chemical processing techniques.

In this thesis, radiochromic films EBT-3 (International Speciality Products, Wayne, USA) with size of 20.3x25.4 cm² and an external flatbed scanner, Epson Dual Lens System-V700 Photo, (Epson, Seiko, Nagano, Japan) with 12-bit pixel depth and resolution 6400 dots per inch are used. Up to date this film is the latest update among the radiochromic films and performs quite well. Some of its advantages are: symmetric structure (eliminates the problem of which side of the film has to be scanned); eliminated Newton's Rings patterns (created from the light reflection between two surfaces located close to each other, one spherical and one flat) and dose rate independency [35]. Its main disadvantage is the lengthy time procedures and very high precision required during its use.

Calibration

For the current measurements, films required calibration prior to any plan irradiation. Film calibration is required in order to convert the optical density into absorbed dose where the dose delivered is related to the darkness of the film. It is defined as shown in equation 8

$$OD = \log(I_0/I_t) \quad (8)$$

Where I_0 is the intensity of light falling on a certain region on the film and I_t is the intensity of light transmitted through the same region. [1.] The film intended for calibration was first digitized by using the Epson scanner. This was done to define the background correction which minimizes the uncertainties during the scanning. The correction factor is calculated by subtracting the pre-exposure values from the post-exposure ones. Next, the same film was cut in 9 equal pieces of 5x5 cm². To create the film response curve, all films were irradiated with known doses. Figure 13 shows the irradiated films. The same physical arrangement was used also for the digitization of them with the scanner. Before irradiation, the known dose to be delivered was planned in TPS for each film. Table 6 presents the assigned MU for each film and the resulted dose in Gy.

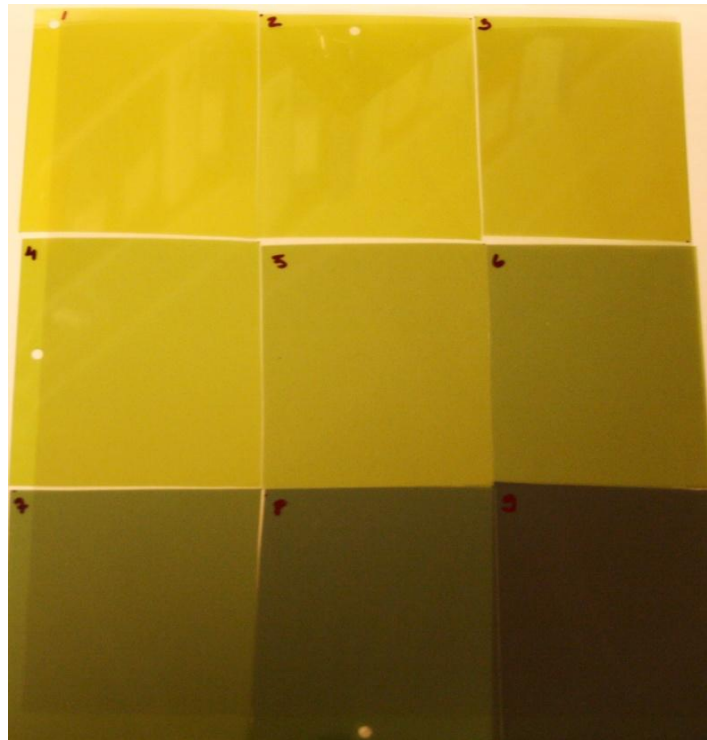


Figure 13. Irradiated films with the known doses in the same arrangement they were scanned.

Table 6. These are the calculated values for each film. The amount of MU dedicated to each of them and the calculated dose delivered accordingly.

Step	1	2	3	4	5	6	7	8	9
MU	0	20	50	90	150	250	400	600	800
Dose (Gy)	0	0.17	0.424	0.764	1.273	2.121	3.394	5.091	6.788

Every film was then irradiated for the planned doses with the Varian linac 6 MV FFF with dose rate 1400 MU/min at SSD of 100 cm and field size of 10x10 cm². One of the scanned films was not exposed to any radiation and is used for fog determination. Each other film was individually inserted within the MCube which was standing on the treatment couch (same setup as in section 3.5.1). The position of the film within the phantom was important to remain static and vacuum free from the surface, during the treatment. Consequently, each film was marked and positioned with regard to the origin

of the phantom. The position of the markers was then used in the film setup, preceding the analysis. The whole process is reliant on film's sensitivity, which depends significantly on the age, type, batch and storage conditions of the film.

Different films have different sensitivities thus the calibrations vary. That is why in the measurement setup, the calibration parameters were stored together with the film type. After the irradiation, films were put in a closed box where they stayed 18 hours until the scanning process. During this time, the active component of the film is polymerized progressively. The amount of polymerization and optical density increases as the dose delivered increases [36]. This explains the different colors observed for each film as shown in figure 13. Film development continues indefinitely, but decreases with time and for acceptable results, there is always a recommended film developing time.

All nine films were digitized by scanning all of them at once at the center of the scanner. In addition, the scanner artefact correction was applied because there was a chance that artefacts are created from the scanner's light during the film scanning. The calibration data were displayed as given in table 7 and saved to the OmniPro I'mRT database. ADC stands for analog-to-digital converter and the shown values were used for such conversion. In addition, based on the results given from Casanova, et al. [35.], each film consists of three main channels, red, green and blue with the red channel having a better response, up to 10 Gy, compared to the green and blue ones. Green channel becomes better than the red one for doses higher than 10 Gy and blue channel does not overtake any of the other two in any case. Keeping in mind that, the only dose/fraction used in the current measurement was 4 Gy, thus the red channel was utilized.

Table 7. Calibration data used for film calibration. Each step (film) is associated with the dose delivered into them and the correspondent analog to digital converter (ADC) value.

Step	1	2	3	4	5	6	7	8	9
ADC	24169	25905	28490	30760	34282	38391	42093	46610	48703
Dose (Gy)	0	0.17	0.424	0.764	1.273	2.121	3.394	5.091	6.788

Dose distribution measurement

After the calibration was complete, the dose distribution of PTV 3 for dose/fraction of 4 Gy was performed. A film from the same batch as the calibration one was picked and a similar procedure as for the calibration was performed. More specifically, the film was digitized on the Epson scanner for fog determination. Then, it was cut in half (sufficient for the current field size) and mounted within the MCube Lite. The phantom itself was positioned on the treatment table exactly as described in section 3.5.1. When the irradiation was completed, the film was put carefully in a closed box. To achieve the best results from film measurements, Aland, et al. [37] suggested that measurement film and calibration film should have the same film developing duration, which was 18 hours.

After 18 hours of film developing (on its own), the film was digitized with the same scanner as before. For every scanning, the scanner was warmed up prior to the scanning. For the reason mentioned before, the red channel of the film was used. Then, the scanned image was imported to OmniPro Im'RT software. The scanner correction factors were calculated from the empty film scanned previously and then they were applied to the image containing the dose distribution. The calibration curve estimated from the calibration process was utilized on the film containing the dose distribution. Finally, the calibrated film was digitally saved and was ready for comparison with the calculated dose distribution.

3.6. Dose distribution evaluations

To provide dose distribution measurements, matrix detector and radiochromic films were used. However, one of the challenges of these methods is the large amount of measured and calculated points and their analysis. Therefore, tools for such analysis have been developed and one of them being the gamma analysis. It is widely used to compare the calculated dose distribution with the measured one for every point [38]. The idea was introduced in 1998 from Low et al. [39] and is based on two different evaluation types, namely *dose difference*, given from equation 9, and *distance-to-agreement* (DTA). The former gives the dose difference of the respective points from both dose distributions as

$$\text{Dose difference} = D_c(r_c) - D_m(r_m) \quad (9)$$

Symbols $D_c(r_c)$ is the calculated dose at r_c in the calculated plan and $D_m(r_m)$ is the dose at r_m in the measured distributed dose. In addition, r_m is the location of a particular measurement point and r_c is the spatial location of the calculated distribution with regard to the measured point, r_m .

On the other hand, DTA gives the distance between a measured dose point and the closest calculated dose point having the same dose value, known also as isodose distance. Keeping in mind the same notations as earlier, DTA is given from equation 10.

$$\delta(r_m, r_c) = D_c(r_c) - D_m(r_c) \quad (10)$$

However, both techniques have their own limitations. The dose difference works well in low gradient regions, but it is not as efficient in high gradient ones because any small misalignment results into a large difference. Whereas, the DTA works correct in high gradient regions (the corresponding dose level is still close by) but not in small gradient ones because it usually takes a large radius to find the matching dose levels even though the misalignment would be small. [1.]

To solve the problem of different sensitivities, a common equation, as shown from equation 11, was developed. It combines the two techniques and is applied for every reference point independently. Because the techniques have their limitations in different dose gradients, this analysis uses one technique in the region where the other tends to be over sensitive and fails to meet the criteria. When both parameters fail, the compared points fail the test.

$$\Gamma(r_m, r_c) = \sqrt{\frac{\delta^2(r_m, r_c)}{\Delta D_M^2} + \frac{|r_c - r_m|^2}{\Delta d_M^2}} \quad (11)$$

and $\gamma(r_m) = \min\{\Gamma(r_m, r_c), \Psi r_c\}$

The first numerator within the square root sign belongs to DTA. The second one corresponds to the dose difference. The threshold Δd_M is for passing the isodose criteria and ΔD_M is for passing the dose threshold. [39.]

After the normalization of both components, Γ is obtained by squaring their values, summing them up and taking its square root, as shown in equation 10. In the end, the gamma index, γ is given as the smallest value of Γ with the distance r changing when the checking is done by going through the isodose line to find the point where DTA is minimal. The deal is that when $\gamma(r_m)$ is equal to or larger than 1, the calculation fails and if $\gamma(r_m)$ is smaller to 1 then the calculation passes. If DTA and dose difference are both on the limit, equal to 1, the test is considered as “fail” because the $\gamma = \sqrt{2}$. In other words, γ provides a single evaluation value, instead of two and it also takes care of the regions where any of the components would perform poorly. [39.]

There is no strict rule in choosing the thresholds for dose difference and DTA because it depends on the case study and relevant experience. However, a general case which is also applied for the comparison of the current calculated and measured data is 3 mm for DTA and 3 % for the dose difference. The size of region of interest (ROI) was 24 by 24 mm, relevant signals ≥ 50 % and search distance 4.5 mm (searching is stopped after 4.5 mm).

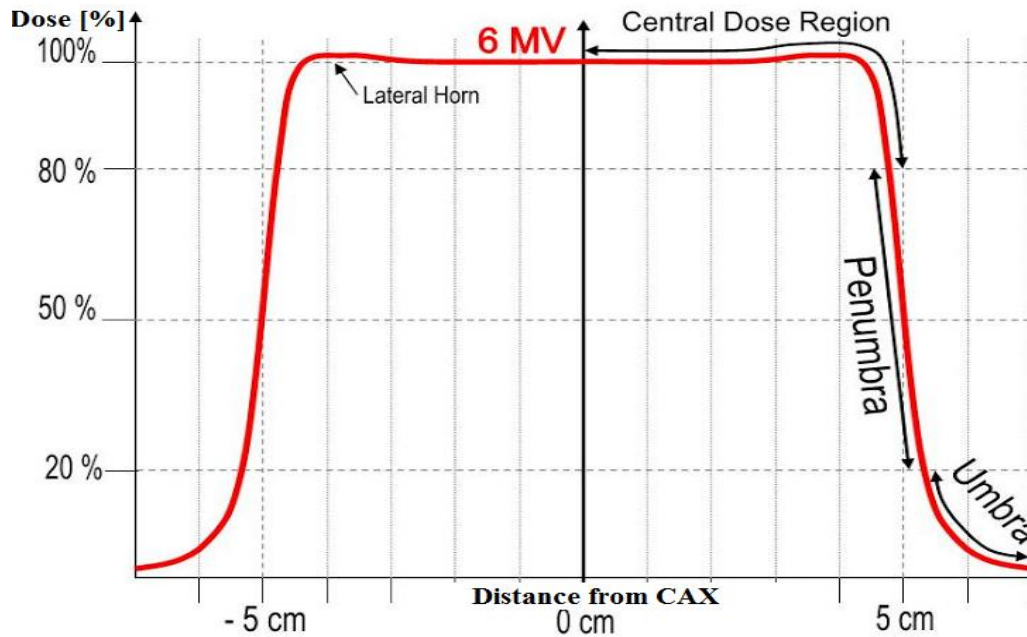


Figure 14. Example of the beam profile and its main components. Adopted from [40].

Gamma analysis gives an overall feedback on the relation between the measured and calculated data. To understand in more detail how well these data fit with each other, dose profile evaluation is needed. Dose profile describes how the dose is altered in the plane perpendicular to the central beam axis at an arbitrary depth. It consists of three main regions, central dose region, penumbra and umbra, as shown in figure 14 [6].

To give a very general evaluation over the comparison between measured and calculated data, accuracy criteria proposed by TRS 398 limitations were used. The difference with gamma analysis is that the latter shows the difference for individual points while TRS 398 is concerned mainly for the disagreement level between measured and calculated dose profiles taken as a whole. TRS 398 concluded that there were no definite exact limitations to be applied for the differences between the data, however, based on experience, the average uncertainties should preferably be within 5%. Finally, the global average uncertainties of all cases should be as well not higher than 5%. [41.] The average uncertainty between measured and calculated data for each case was generated by converting the grid size of calculated data to 0.7619 cm resolution and keeping the grid size of measured data unchanged (by default was 0.7619 cm). This conversion was made so the calculated data had the same spatial resolution as the measured one. Finally, the dose difference was estimated in different points of the high dose regions and their average value was calculated.

4. RESULTS

4.1. Calculated dose distributions

Dose conformities together with the dose-color legend for both PTVs for dose/fraction of 4 Gy and 18 Gy are given in figures 15 through 18. PTV volume is represented by the outer red contour and the respective GTV with the inner contour. From the thesis perspective, one could notice that dose distributions within the target seem to be quite conforming. Dose is concentrated within the target and RTOG requirements were met: maximum dose in PTV was between the required limits of 110 % and 140 % of the prescribed dose and the volume of 105 % of the prescribed dose outside the target did not exceed the threshold of 15 % of the PTV volume. This was the case for all plans and for display purposes PTVs with the lowest (4 Gy) and highest dose/fractions (18 Gy) are presented only (figure 15-18).

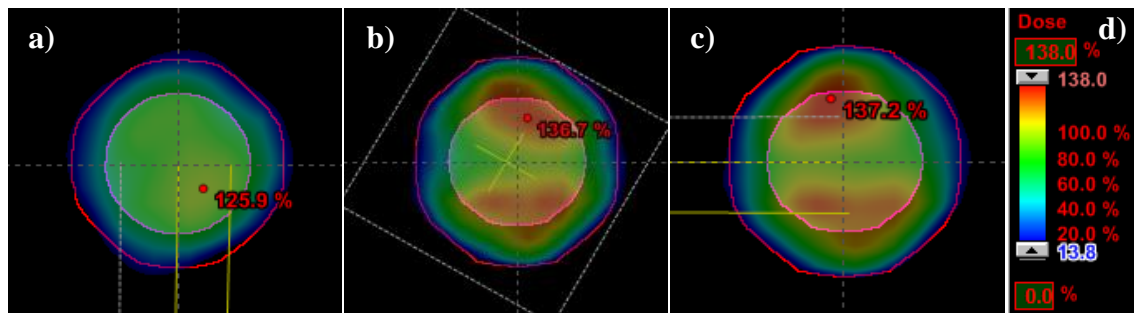


Figure 15. Dose conformity in PTV 3 for dose/fraction of 4 Gy. PTV is modelled as the outer contour and GTV as the inner one. Viewing planes are a) transversal, b) frontal and c) sagittal. The percentage shows the maximum dose within the volume which is within the RTOG limits. The maximum dose in percentage a) 125.9 %, b) 136.7 %, c) 137.2 % shows the maximum dose within the target volume which were within the RTOG limits and d) gives the color legend corresponding to the prescribed dose.

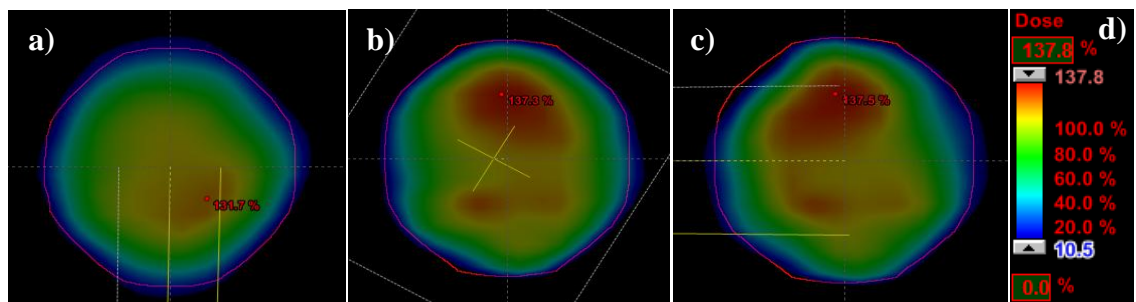


Figure 16. Dose conformity in PTV 3 for dose/fraction of 18 Gy. PTV is modelled as the outer contour and GTV as the inner one. Viewing planes are a) transversal, b) frontal and c) sagittal. Percentage a) 131.7 %, b) 137.3 %, c) 137.5 % shows the maximum dose inside the target volume, which were within the RTOG limits; d) gives the color legend corresponding to the prescribed dose.

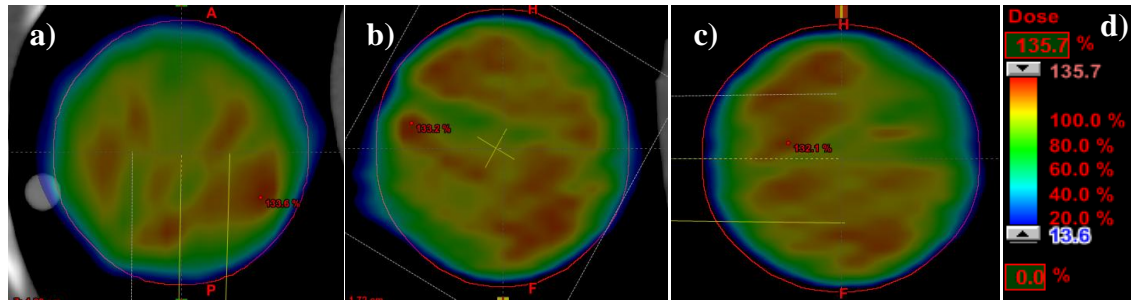


Figure 17. Dose conformity in PTV 6 for dose/fraction of 4 Gy. PTV is modelled as the outer contour and GTV as the inner one. Viewing planes are a) transversal, b) frontal and c) sagittal. Percentage a) 133.6 %, b) 133.2 %, c) 132.1 % shows the maximum dose inside the target volume, within RTOG limits and d) gives the color legend corresponding to the prescribed dose.

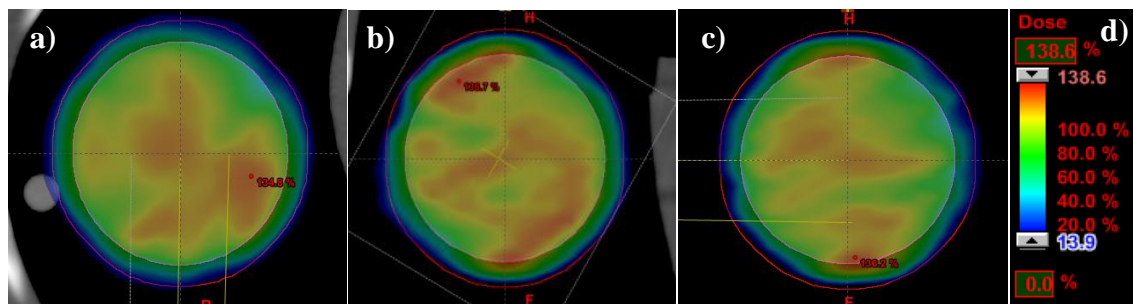


Figure 18. Dose conformity in PTV 6 for dose/fraction of 18 Gy. PTV is modelled as the outer contour and GTV as the inner one. Viewing planes are a) transversal, b) frontal and c) sagittal. Percentage a) 134.8 %, b) 136.7 %, c) 136.2 % shows the maximum dose inside the target volume, within RTOG limits and d) gives the color legend corresponding to the prescribed dose.

The hot spots usually seen in the target volumes are considered to be positive as long as they are within the GTV and do not reach the normal tissues. The ones located in the center of the volume are even better because of their high efficiency to break the resistance of the tumor, most likely situated within the same region. [2.]

DVHs displayed in figure 19 and 20 show the uniformity of the dose within the PTV and GTV. The steeper the PTV graphs the better dose uniformity. Figure 19 corresponds to PTV 3 (red) and its respective GTV (pink); the relative dose in percentage is given with regard to the structure volume also expressed in percentage. For display purposes, cases of 4 Gy and 7.5 Gy were combined together and the ones of 11 Gy and 18 Gy were combined in one graph. The same was applied for PTV 6 and its respective GTV in figure 20. As it can be observed, for each case, the RTOG requirements were met: 95 % of the target volume (PTV) receives 100 % of the prescribed dose and 99 % of the volume receives at least 90 % of the prescribed dose.

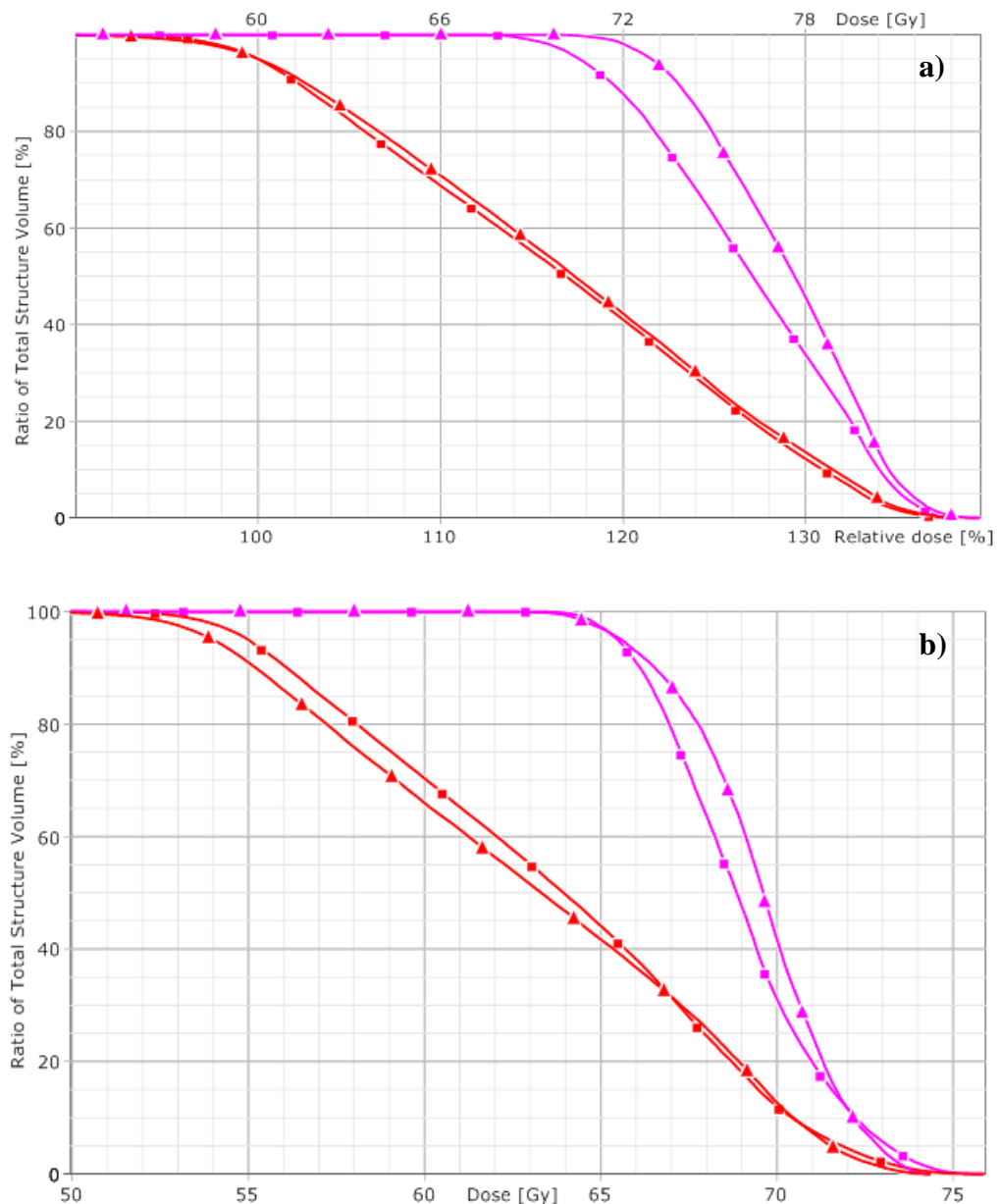


Figure 19. The combined histograms for PTV 3 (red) and the respective GTV (pink). The dose/fractions for each of them are a) \blacksquare =4 Gy and \blacktriangle =7.5 Gy, b) \blacksquare =11 Gy and \blacktriangle =18 Gy. RTOG protocol requirements were met.

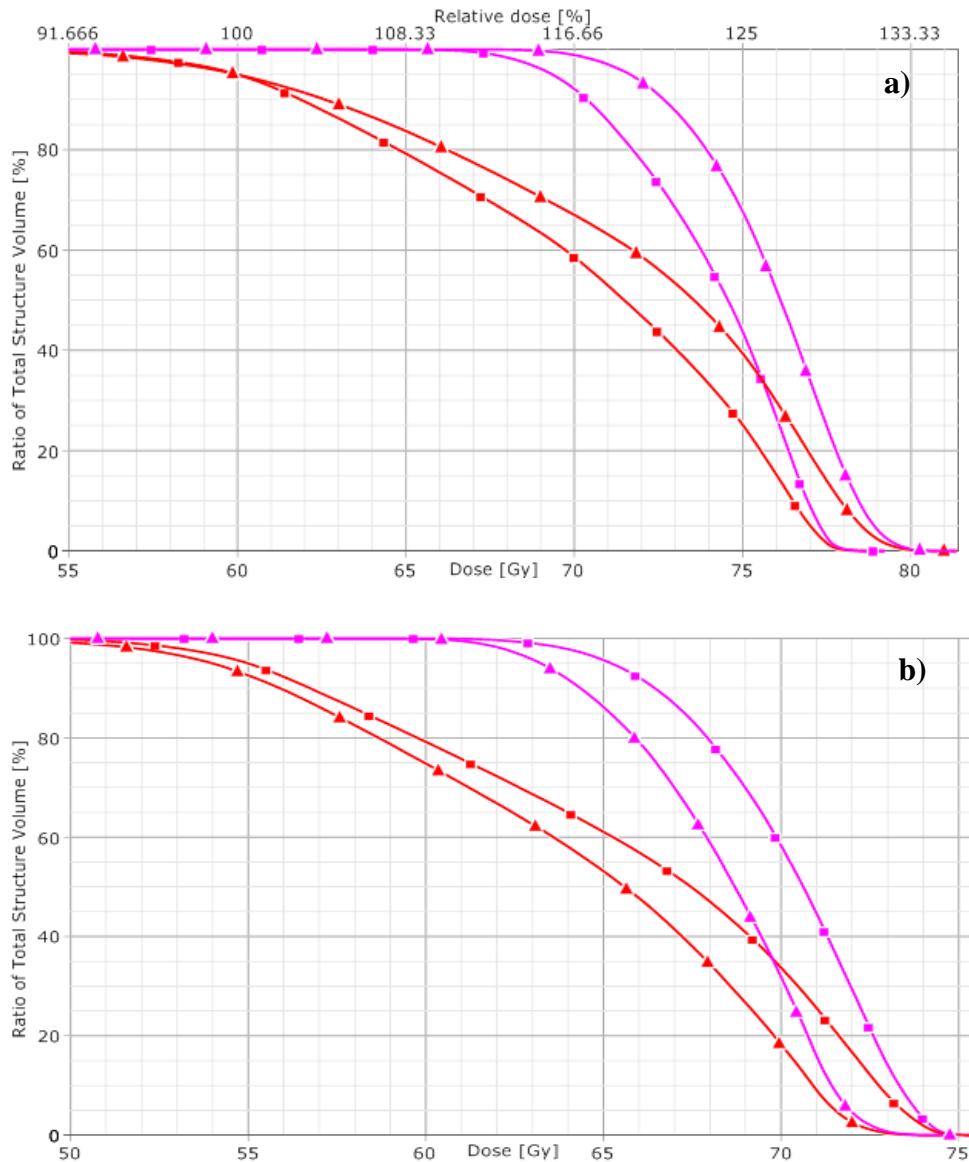


Figure 20. The combined histograms for PTV 6 (red) and the respective GTV (magenta/pink). The dose/fractions for each of them are a) ■ stands for 4 Gy and ▲ stands for 7.5 Gy, b) ■ represent 11 Gy and ▲ represent 18 Gy. RTOG protocol requirements were met.

4.1.1. Delivery time and the amount of monitor units

The time required for the delivery of the prescribed dose and the amount of monitor units used for each PTV are given in table 8. As it is expected, for the same PTV, higher the dose/fraction, longer the delivery time. The same can be concluded when the dose/fraction remained unchanged and PTV diameter increased. It was noticed that if the same dose/fraction is used for the two different PTVs then there is a small time advantage when small PTV was irradiated. The dose delivery time for each case was considered as clinically acceptable.

Table 8. Results concerning the amount of monitor units (MU) and delivery time (min) for each PTV and dose/fraction.

PTV_Dose/Fraction	3_4	3_7.5	3_11	3_18	6_4	6_7.5	6_11	6_18
Monitor Units, MU	913	2286	2337	3885	1025	1761	2501	3930
Time, min	0.66	1.14	1.67	2.78	0.75	1.26	1.79	2.81

4.2. Dosimetric verifications

4.2.1. Matrix detector on treatment couch

Results gained from the matrix detector were in general acceptable, especially for the large field sizes (from PTV 6). The dose level of measured profile was in very good agreement with the calculated one for PTV 6 but not as good for PTV 3 where smaller field sizes were used. This can be checked both visually and numerically (average dose differences collected for the high dose region of the signal). These values for PTV 6, based on the TRS 398 protocol, were generally within the suggested limits while for PTV 3 were slightly above these limits. The reason why these average values are not smaller was because of some peak deviations in the corners of high dose region. Details for each case are explained next.

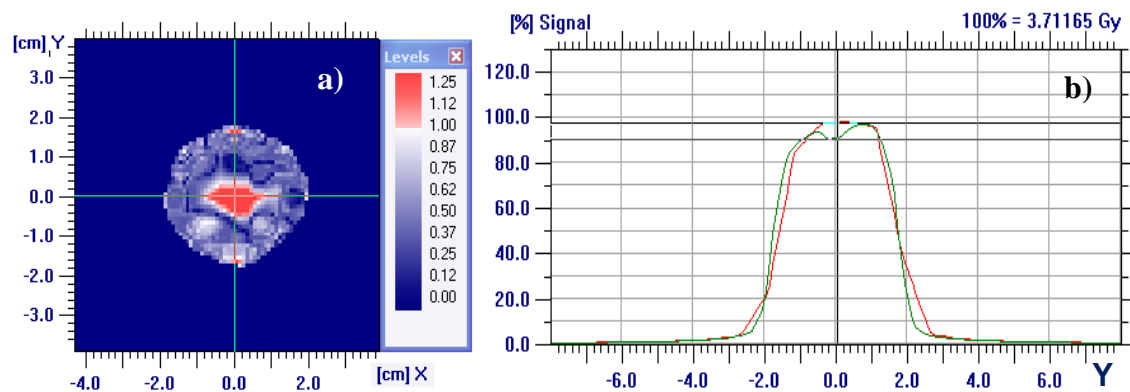


Figure 21. a) Gamma analysis for the compared data corresponding to PTV 3 and dose/fraction=4 Gy b) direct comparison between measured (red) and calculated (green) dose profiles in Y-direction. Dose difference at the center of the dose map was at maximum of 7.5 % and the average dose difference calculated for the signal above 90 % was 6.0 %.

Figure 21a) presents the gamma analysis of the measured and calculated results for the PTV 3 irradiated with 4 Gy/fraction. As the legend in the figure illustrates, gamma values larger than 1 are marked as fail (red), pass if smaller than 1. Meanwhile figure 21b) demonstrates the profile comparisons between measured (red) and calculated (green) results. Here, only the profiles in the Y-direction are illustrated because of the higher differences observed compared to the ones in the X-direction. These profiles are the ones seen from Y-direction at position (0, 0) in the 2D dose gamma map. Furthermore, one can also notice which part of the profiles are relevant to the gamma analysis, merely by synchronizing the Y-axes of both figures. Thus, as seen from both figures, the major disagreements, given in red, come from the central dose region where the

peak difference (measured-calculated) between the data was 7.5 %. Yet, the average dose difference calculated for ROI occupying high dose region of the signal was 6.0 %.

Figure 22 reveals information for PTV 3 and dose/fraction of 7.5 Gy. According to gamma analysis, the disagreement comes from the high dose region of the profiles where the maximum dose difference reaches up to 8 %. The average dose difference was about 7.6 % which was above the suggested limit as well.

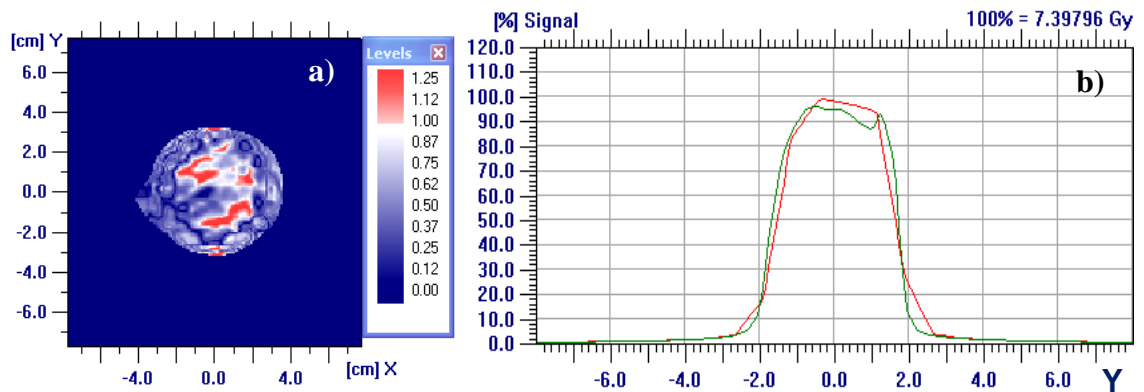


Figure 22. a) Gamma analysis for the compared data corresponding to PTV 3 and dose/fraction=7.5 Gy b) direct comparison between measured (red) and calculated (green) dose profiles in Y-direction. Dose difference at the center was about 8% and the average dose difference calculated for the high dose region of the signal was 7.6 %.

Figure 23 shows the dose distribution comparison for PTV 3 and dose/fraction equal to 11 Gy. The situation seems to be similar to the previous ones, in which the main difference is located in the high dose region while the rest appeared to have better agreement. The dose difference in the centre is about 6.5 %, in the lateral horns varies from 3.3 to 6.6 %. These maximal disagreements were large enough to generate inadequate average value of 5.2 %, calculated for the high dose region.

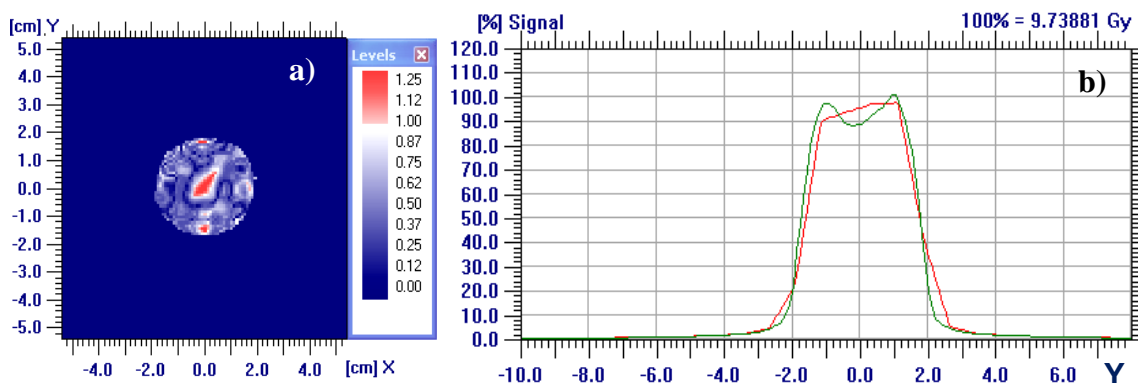


Figure 23. a) gamma analysis for the compared data corresponding to PTV 3 and dose/fraction=11 Gy b) direct comparison between measured (red) and calculated (green) dose profiles in Y-direction. Dose difference at central area is about 6.5 %, at the lateral horns varied between 3.3 and 6.6 % and average dose difference equal to 5.2 % for ROI occupying the high dose region of the signal.

Images of figure 24 correspond to PTV 3 and dose/fraction of 18 Gy. The same phenomena was noticed, the failed agreement was located in the central area of the gamma map, central dose region, with approximated dose difference equal to 4.3 %. On the other hand, the average value of disagreement for ROI covering high dose region of the signal was 5.8 %.

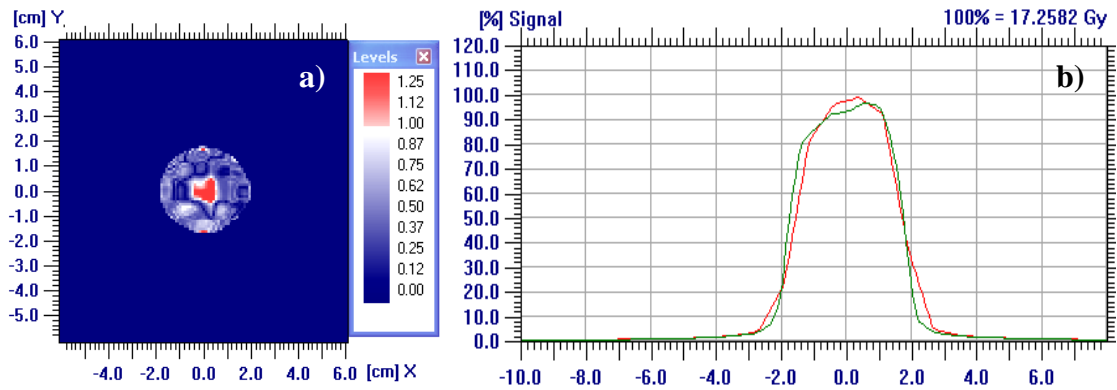


Figure 24. a) gamma analysis for the compared data corresponding to PTV 3 and dose/fraction=18 Gy b) direct comparison between measured (red) and calculated (green) dose profiles in Y-direction. Dose difference at the center was about 4.3 % with the average one being 5.8 % for ROI covering the high dose region of the signal.

The dose distribution comparison, gamma analysis associated with an example containing the dose profiles of measured and calculated data for PTV 6 and dose/fraction equal to 4 Gy is shown in figures 25. Both images show that the disagreements appear to be concentrated in almost the whole central dose region. This can be verified by simply checking the location of this region in the profile, being roughly between -3 and 3 cm in the Y direction and comparing it with the same region in the gamma map, where one can see that roughly in the same region and direction the red area is. The differences in the central dose region ranged between 3.5 % and 5.5 % and in the lateral horns it varied between 1.2 % and 3.5 %. These peak values together with other ones in the high dose region generated an acceptable average dose difference of 4.7 %.

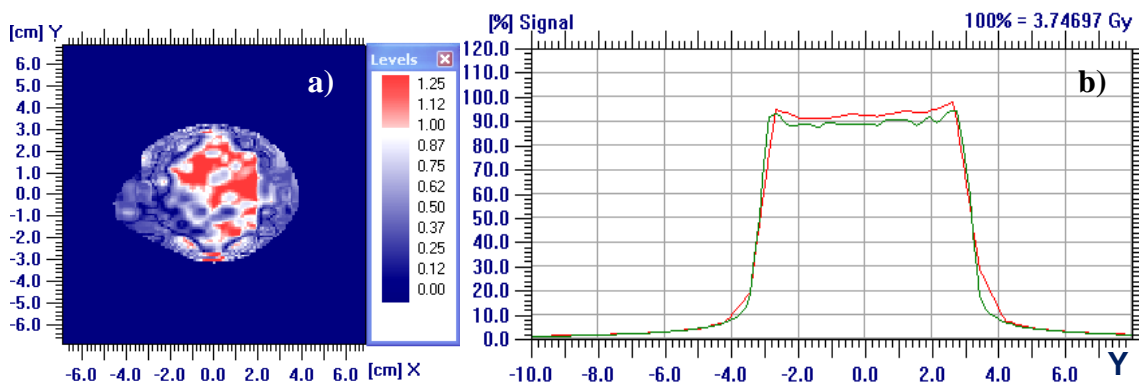


Figure 25. a) gamma analysis for the compared data corresponding to PTV 6 and dose/fraction=4 Gy b) direct comparison between measured (red) and calculated (green) dose profiles in Y-direction. Dose difference at the center was between 3.5 and 4.5 % while in the lateral horns varied between 1.2 and 3.5 %. Average dose difference was 4.7 % for ROI concentrated above 87% of the signal.

Figures 26, 27, 28 show the results for dose/fraction of 7.5 Gy, 11 Gy and 18 Gy applied on PTV 6, respectively. Dose differences for the case of dose/fraction equal to 7.5 Gy were mainly between the central axis and the lateral horns, about 6 % in both sides, as illustrated from the obvious discrepancy in figure 26. The average one was 3.6 % considering ROI above 90 % of the signal.

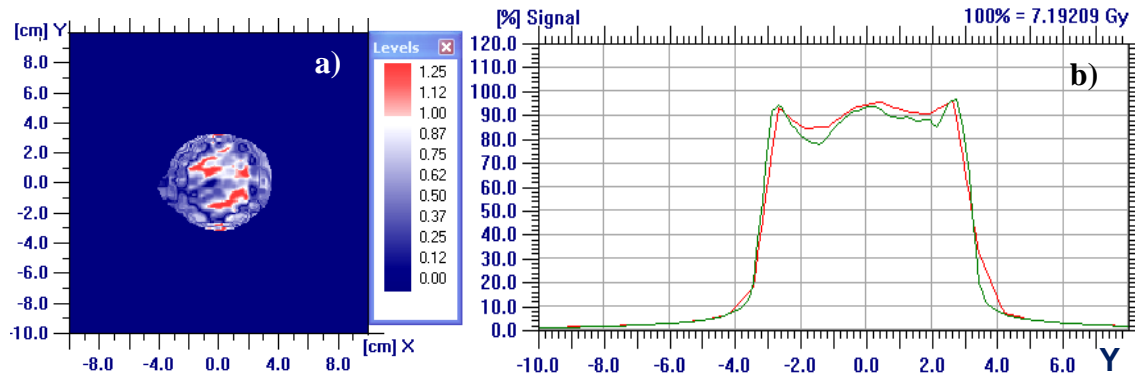


Figure 26. a) Gamma analysis for PTV 6 and dose fraction of 7.5 Gy and b) direct comparison between measured (red) and calculated (green) dose profiles in Y-direction. Dose difference at the center was low between 3.5 and 4.5 % while in the lateral horns reached about 6 %. Average dose difference was at the acceptable level of 3.6 % for ROI of above 90 % of the signal.

For the case of 11 Gy, given in figure 27, the dose differences between the measured and calculated results were concentrated in the central dose region and were similar to the previous case with the maximum reaching at 6 % in the high dose region. However, the average dose difference was 4.5 % for ROI being above 90 % of the signal.

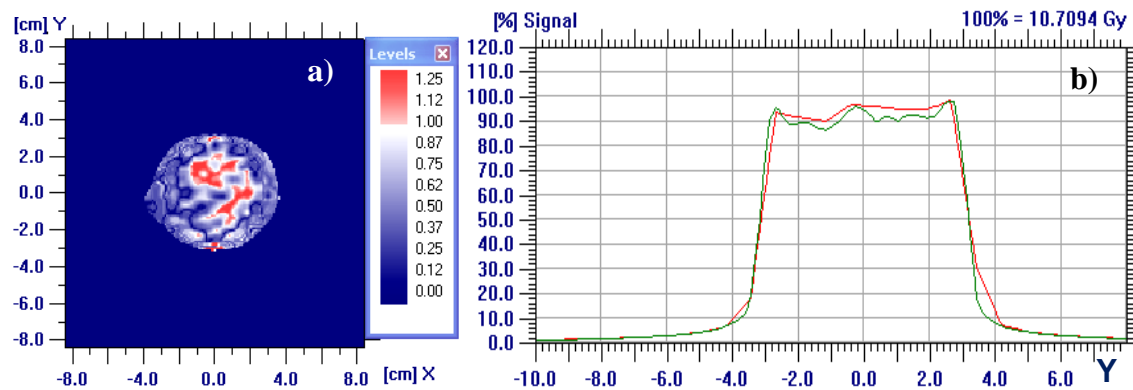


Figure 27. a) Gamma analysis for PTV 6 and dose fraction of 11 Gy and b) direct comparison between measured (red) and calculated (green) dose profiles in Y-direction. Dose difference at the center was on average about 3.5 % while in the lateral horns was negligible. Average dose difference was 4.5 % for ROI of above 90 % of the signal.

Finally, the last case concerning PTV 6 and dose/fraction of 18 Gy is given in figure 28. The same pattern as for the previous cases of PTV 6 was observed. The main dose difference concentrated on the high dose region, with the maximum reaching 5.2 % and the average being 3.8 % for ROI above 90 % of the signal.

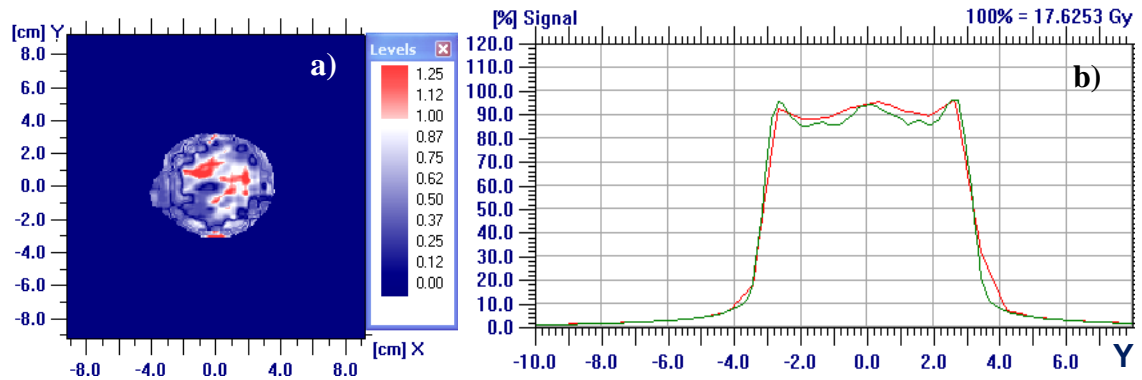


Figure 28. a) Gamma analysis for PTV 6 and dose fraction of 18 Gy and b) direct comparison between the dose profiles of measured (red) and calculated (green) in Y-direction. Dose difference at the center was on average about 3.5 % while in the lateral horns was negligible. Average dose difference was 3.8 % for ROI higher than 90 % of the signal.

4.2.2. Matrix detector mounted on treatment head

Results shown next are from the measurements done with MXX mounted on the gantry. Gamma analysis with regard to PTV 3 and dose/fraction of 4 Gy is illustrated in figure 29a). Figure 29b) reveals the comparison between the profiles in Y-direction. Results demonstrated that the major disagreements between measured (red) and calculated (green) data came from the central dose region, including lateral horns and central area. Dose differences between the data were 8-9.5 % in the lateral horns and about 6 % in the central area. In general these values were unacceptable and so was the average dose difference, 6.2 % noticed for ROI above 90 % of the signal.

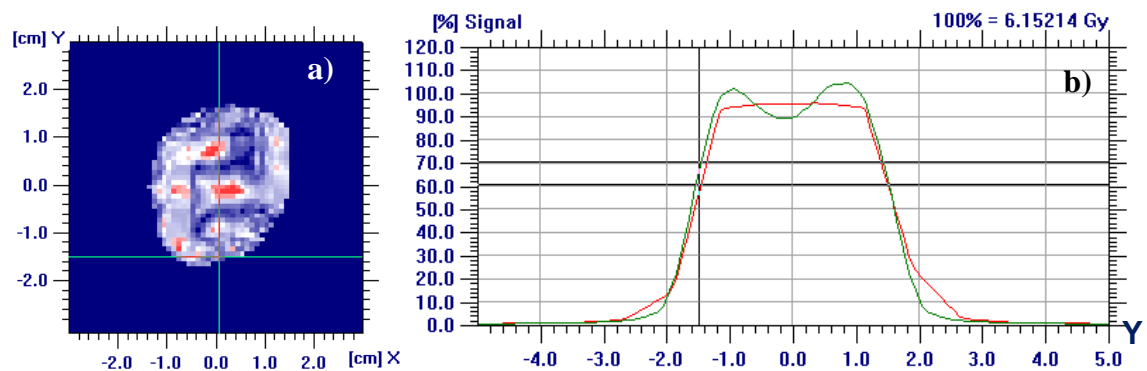


Figure 29. a) Gamma analysis of the compared data for PTV 3 and dose/fraction=4 Gy, b) direct comparison between measured (red) and calculated (green) dose profiles in Y-direction with dose differences 6 % and 8-9.5 % at the center and lateral horns, accordingly. Average dose difference was 6.2 % for ROI higher than 90 % of the signal.

Figure 30 gives the compared results for PTV 3 and dose/fraction of 7.5 Gy. Obviously, the difference between measured and calculated data was negligible and certainly within the acceptable suggested limits. However, the average dose difference for the high dose region, calculated as explained in chapter 3.6, gave a contradictory value of 6.2 %. Figure 30c shows the dose levels from which the average dose difference was calculated. It is obvious that these two graphs have significant differences between each other. Two main reasons were thought to explain such contradiction. First one was thought to be the different grid size of the calculated data. In figure 30b the grid spatial resolution was 0.1 cm and in figure 30c it was 0.7619 cm. The linear interpolation used in these different grid sizes produced irrational results, especially for small field sizes. The second reason was the poor resolution of the matrix detector, combined as well with the small field size. A study related to the first problem is currently going on in the clinic and initial results had supported such dependency.

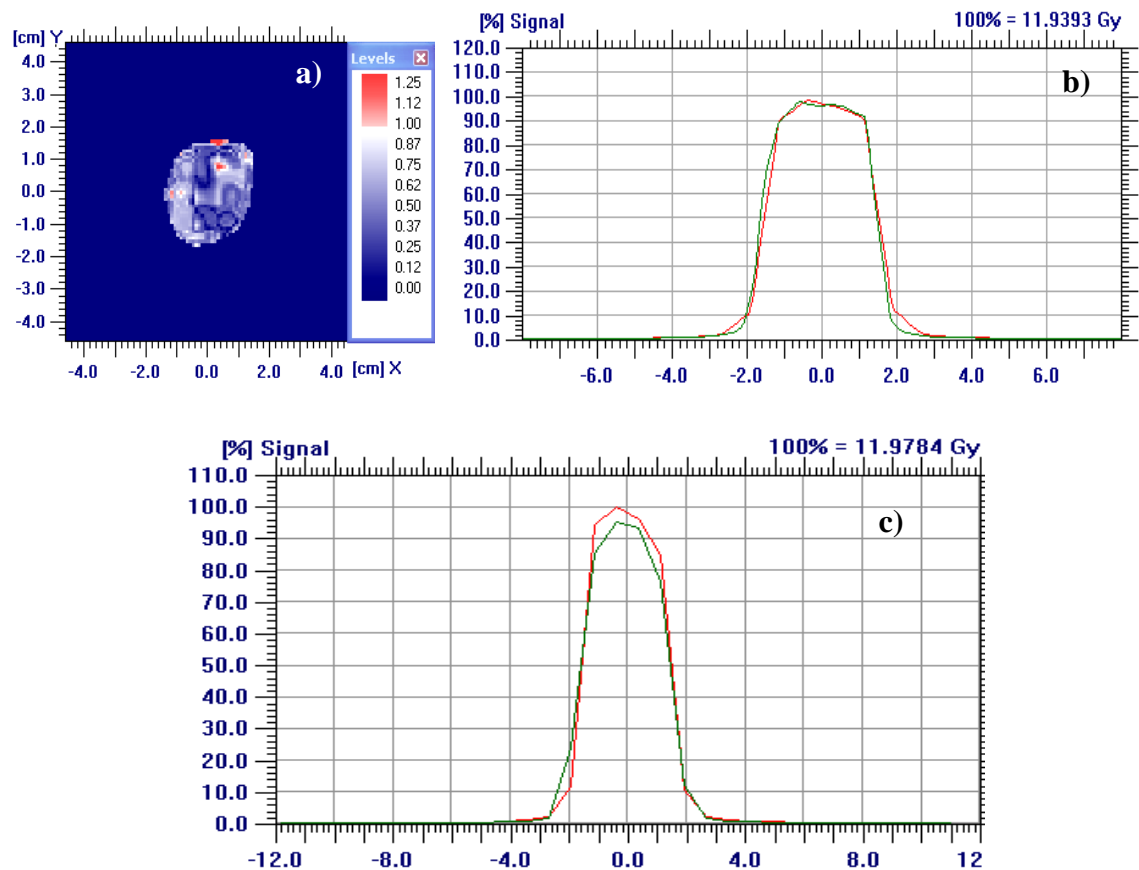


Figure 30. a) Gamma analysis of the compared data for PTV 3 and dose/fraction=7.5 Gy, b) direct comparison between measured (red) and calculated (green) dose profiles in Y-direction. There is no significant discrepancy between them and the grid size was 0.1cm c) the dose profiles from which the average dose difference, 6.2 %, was calculated for the high dose region of the signal. Grid size was 0.7619 cm.

Figure 31 gives the results for the compared data concerning PTV 3 and dose/fraction of 11 Gy. Results are similar to the case of 4 Gy of the same PTV (figure 29). Hence, the problem remains the same; the disagreements come from the central dose region: central part and lateral horns. The dose differences for dose/fraction of 11 Gy with regard to the central area and lateral horns were 4 % and about 9.5 %, accordingly and the average dose difference was 7 % for ROI covering high dose region of the signal.

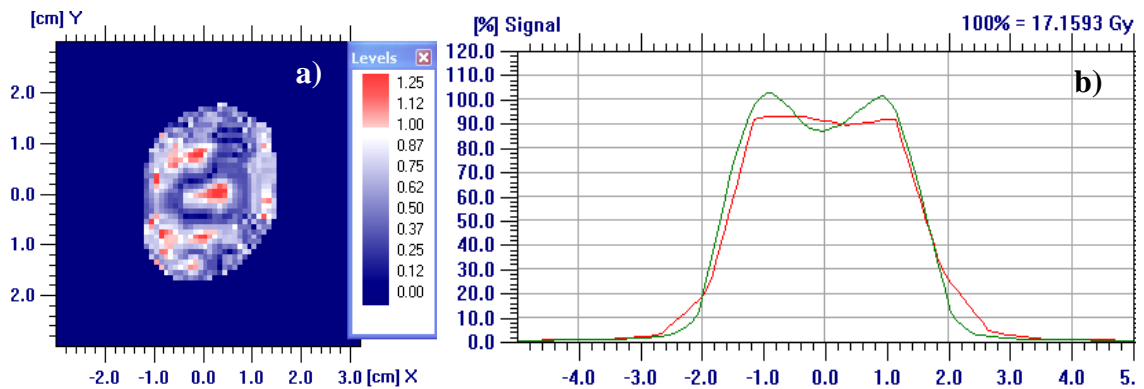


Figure 31. a) Gamma analysis of the compared data for PTV 3 and dose/fraction=11 Gy. b) a direct comparison between the dose profiles of measured (red) and calculated (green) in Y-direction. Dose differences at the central area was 4 % and at lateral horns about 9.5 %. Average dose difference was 7 % for ROI of high dose region of the signal.

As for the dose/fraction equal to 18 Gy, given in figure 32, the differences were slightly smaller than previously, 3.5 % and 8.5 % to the central area and lateral horns, accordingly. The average dose difference was at unacceptable levels of 6.7 % for ROI of high dose region of the signal.

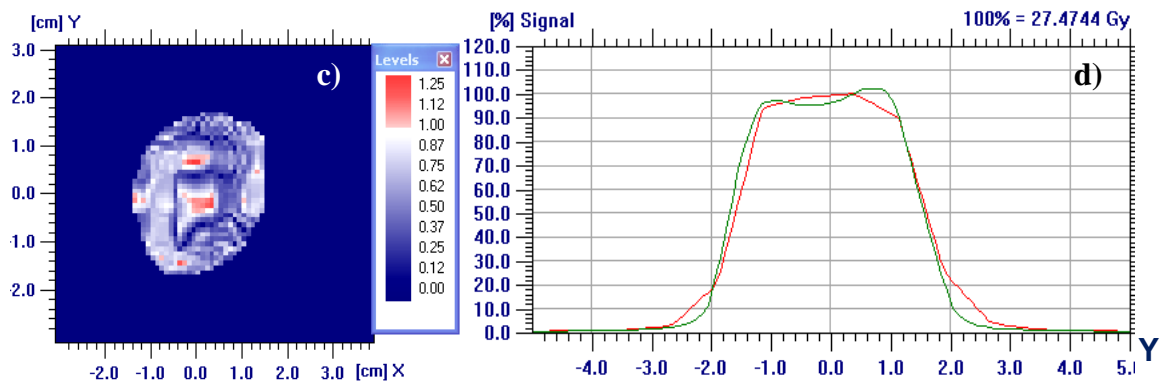


Figure 32. a) Gamma analysis of the compared data for PTV 3 and dose/fraction=18 Gy. b) direct comparison between measured (red) and calculated (green) dose profiles in Y-direction. Dose differences of 3.5 % and 8.5 % were recorded at the center and lateral horns, respectively. Average dose difference was 6.7 % for ROI covering the high dose region of the signal.

Figures 33 through 36 illustrate results regarding PTV 6 for dose/fractions of 4 Gy, 7.5 Gy, 11 Gy and 18 Gy, respectively. As it can be noticed, the problem was the same as in the previous results. The main dose differences came from the high dose region (center and lateral horns). Dose differences for dose/fraction of 4 Gy at central region and lateral horns were approximately 3 % and 7-8.5 %. Average dose difference was estimated to be 4.5 % for ROI above 80 % of the signal, which was still within the suggested TRS 398 standards.

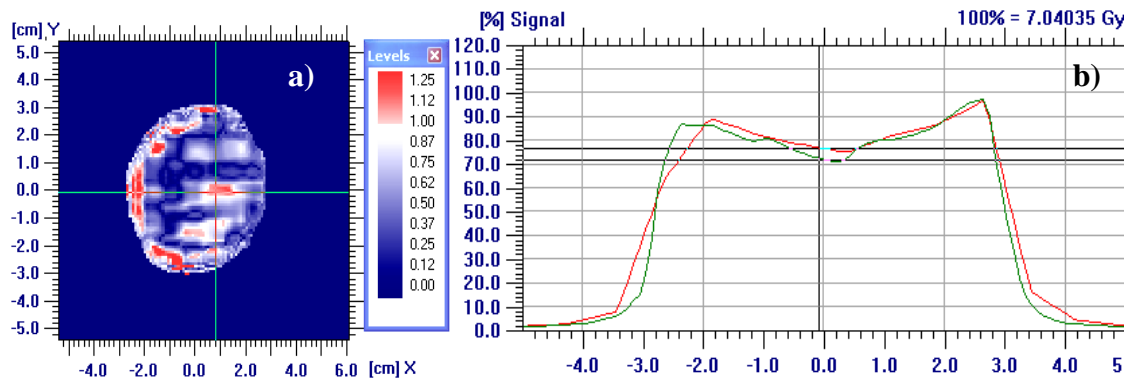


Figure 33. a) Gamma analysis of the compared data for PTV 6 and dose/fraction=4 Gy, b) direct comparison between measured (red) and calculated (green) dose profiles in Y-direction as shown from the crosshair in the dose map. Dose differences in percentage for central region and lateral horns are 3 % and 7-8.5 %, accordingly. Average dose difference was 4.5 %.

Dose differences for PTV 6 and dose/fraction of 7.5 Gy, in figure 34, appeared to be quite similar to the previous case. Dose differences at central region and lateral horns were approximately 1-4 % and 7-8 %. Average dose difference was estimated to be 4 % for ROI of high dose region.

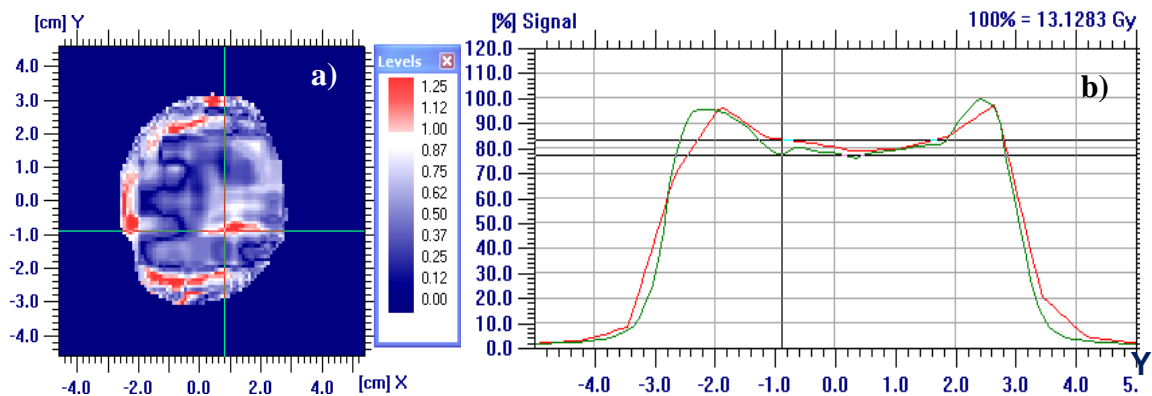


Figure 34. a) Gamma analysis of the compared data for PTV 6 and dose/fraction=7.5 Gy b) direct comparison between the dose profiles of measured (red) and calculated (green) in Y-direction. Dose differences in percentage for central region and lateral horns are 1-4 % and 7-8 %, respectively. Average dose difference was 4 % for ROI covering high dose region.

Figure 35 illustrates dose differences for PTV 6 and dose/fraction of 11 Gy. These differences at the central region and lateral horns were between 0.5-6 % and 5-11 %. Even though, these peak values are above the suggested limits, average dose difference was still alright and was estimated to be 4 % for ROI above 90 % of the signal.

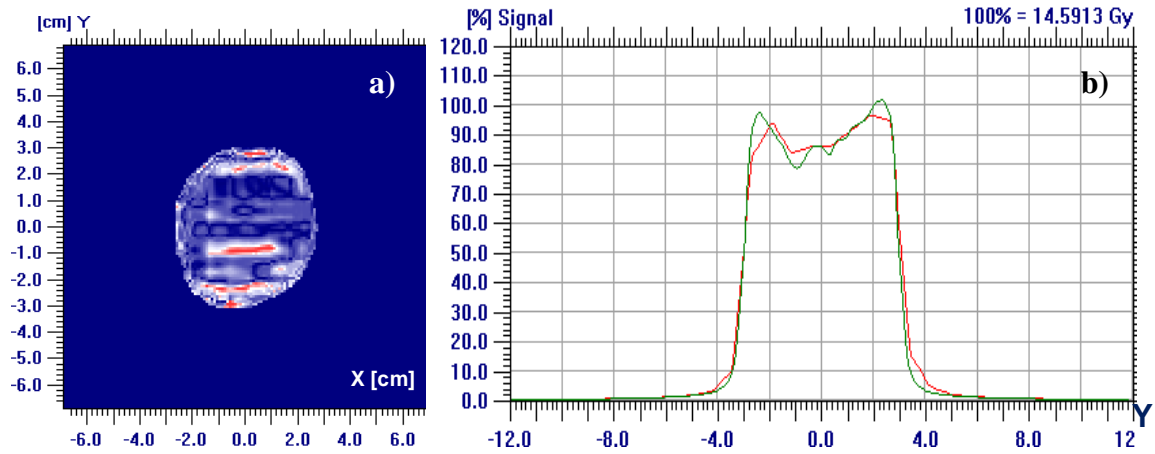


Figure 35. a) Gamma analysis of the compared data for PTV 6 and dose/fraction=11 Gy, b) direct comparison between the dose profiles of measured (red) and calculated (green) in Y-direction. Dose differences in percentage for central region and lateral horns are 0.5-6 % and 5-11 %, accordingly. Average dose difference was 4 % for ROI above 90 % of the signal.

Figure 36 shows dose differences for PTV 6 and dose/fraction of 18 Gy. As it can be noticed, main differences at central region were between 1.5-5 % and at lateral horns was 5-10 %. Average dose difference was estimated to be 4.16 % for ROI above 90 % of the signal. Table 10 gives a summary of the dose differences in the central region, lateral horns and their averages for each measured case.

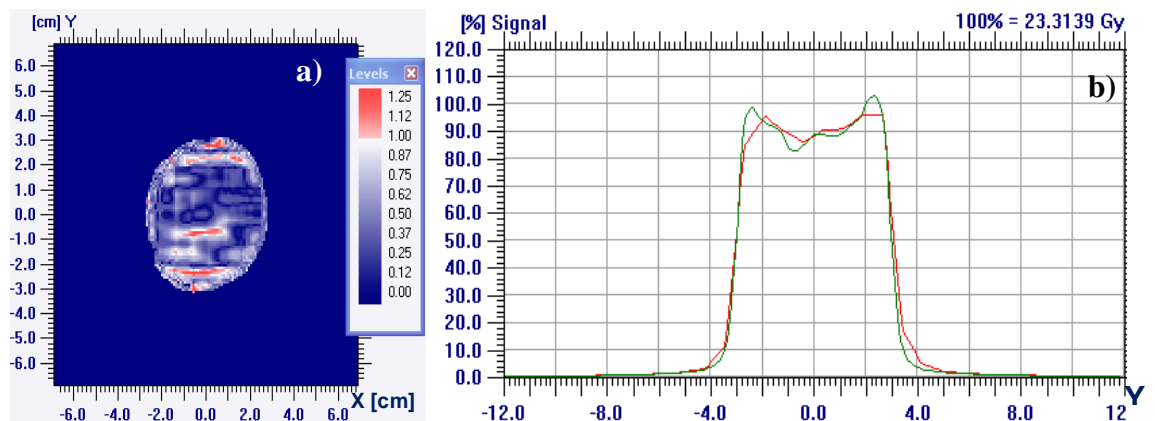


Figure 36. a) Gamma analysis of the compared data for PTV 6 and dose/fraction=18 Gy, b) direct comparison between the dose profiles of measured (red) and calculated (green) in Y-direction. Dose differences in percentage for central region and lateral horns are 1-5.5 % and 5-10 %, accordingly. Average dose difference was 4.16 % for ROI above 90 % of the signal.

Table 9. Summary of the deviations at the central region and lateral horns for both PTVs and applied dose/fractions for both detector setups. Average values are added for each setup. Global average is generated from all the averages of the respective setup.

PTV_dose/fraction	MXX-Mcube			Gantry-mounted MatriXX		
	central region within	lateral horns within	Average [%]	central region within	lateral horns within	Average [%]
3_4	7.5 %		6	6 %	8-9.5 %	6.2
3_7.5	8 %		7.6	N*	N*	6.2
3_11	6.5 %	3.3-6.6 %	5.2	4 %	9.5 %	7
3_18	4.3 %		5.8	3.5 %	8.5 %	6.7
	Average of the PTV		6.2			6.5
6_4	3.5-5.5 %	1.2-3.5 %	4.7	3 %	7-8.5 %	4.5
6_7.5		6 %	3.6	1-4 %	7-8 %	4
6_11	6 %		4.5	0.5-6 %	5-11 %	4
6_18	5 %		3.8	1-5.5 %	5-10 %	4.2
	Average of the PTV		4.2			4.2
	Global average		5.2			5.4

* N stands for "Negligible" values.

4.2.3. Film measurement

Finally, the film measurement results are shown in figure 37. The red profile shows the measured data and the green one shows the calculated data for PTV 3 and dose/fraction of 4 Gy. It is clear that the absolute dose difference in dose level is quite high, at about 10 % but the shape of the profile is very similar to the calculated one, as displayed in figure 38. Therefore results in terms of of the dose profile can be considered acceptable.

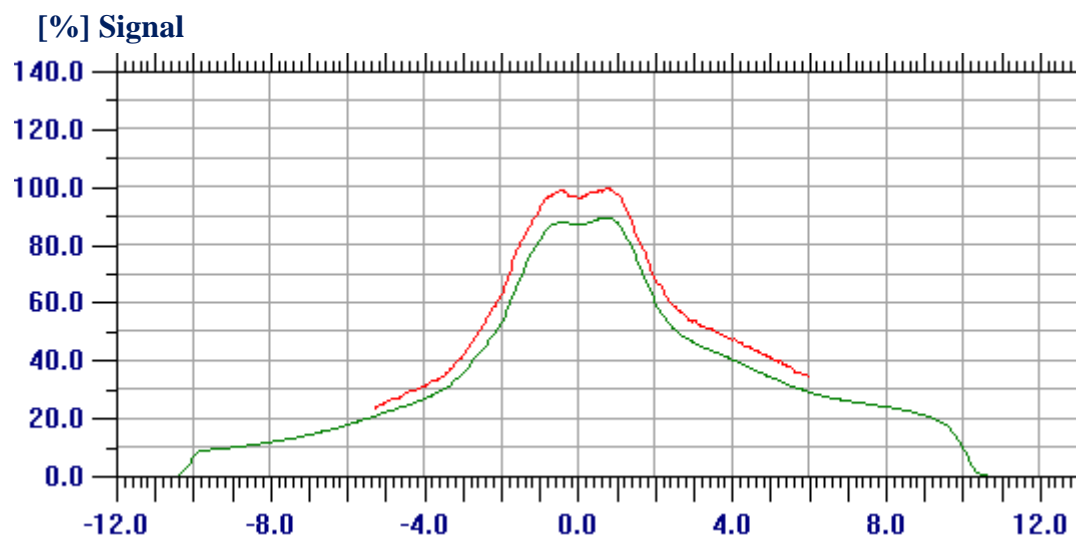


Figure 37. Comparison between measured (red) and calculated (green) profiles for PTV 3 and dose/fraction=4 Gy at Z-direction. It is clear that the difference among them is about 10 %.

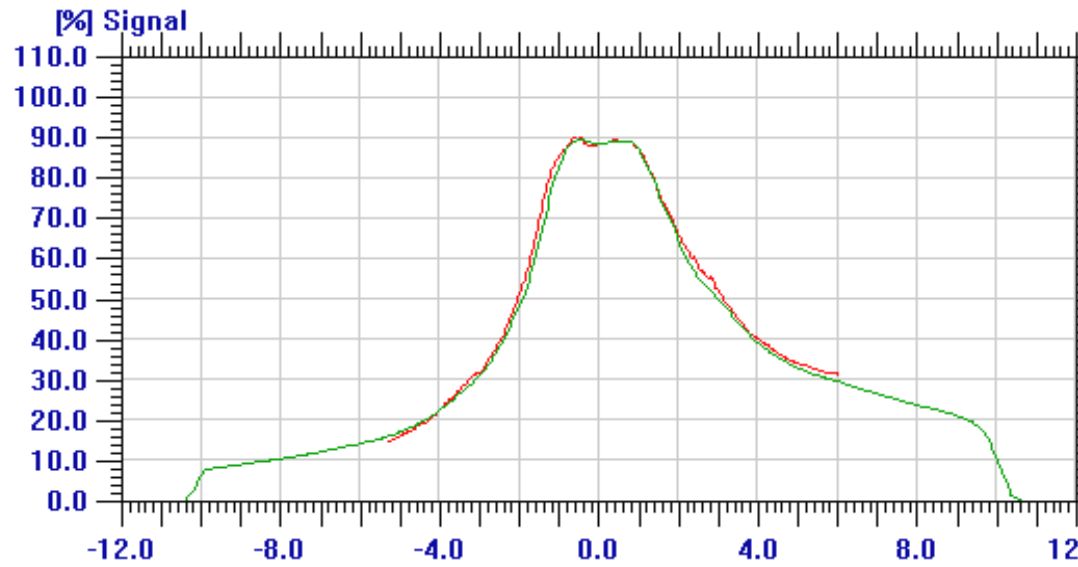


Figure 38. Relative dose comparison. Dose profile shapes between measured (red) and calculated (green) data are in very good agreement.

Film measurements for other cases were not implemented because of the unsatisfactory results from the current case. Reasons for such gap between the data are discussed in the coming chapter.

5. DISCUSSION

5.1. Dose within the target volume

From the results presented in this thesis, one could notice that dose delivery within the target has been satisfactory. The RTOG requirements were met by simply performing few optimization iterations and slight modifications of the objectives for each structure. The hotspots were all within the PTV and in most cases even inside the GTV. These prominent results were further supported by the outcomes of dose-volume histograms where the PTV and GTV both obeyed the RTOG protocol rules. An important role in the well dose distribution was played by the dose fall-off gradient. Parameters that influence the fall-off gradient are the beam energy and MLC leaf width. For small beams commonly used in SBRT, the larger the beam energy, the larger the beam penumbra broadening due to increased lateral electron transport in medium. Considering that lung tissue is a medium of low density, this relationship is emphasized even more. The 6 MV beam used in this case was a good trade-off between beam penetration power and penumbra quality. As for the MLC, higher the spatial resolution, better the dose distribution is. However, this relation is limited by the finite source size and lateral range of secondary electrons. For tumors with diameter larger than 3 cm, the MLC leafs employed by the current linac has been considered to be reasonable [2].

Another factor contributing in the uniformity of the dose in the target is the avoidance of the organs at risk surrounding the PTV. The introduction of many OARs in the optimization process would increase the difficulty of the calculation for the algorithm. For example there are tissues with various electron densities, such as hard tissue (for example ribs) and soft tissue (for example lungs, heart, and oesophagus) that increase the calculation difficulty. Even though it depends on the geometry, energy and number of chosen beams, the more different healthy tissues involved, the more complicated the algorithm calculation becomes. It does not necessarily mean that the dose distribution becomes worse but definitely it would be more challenging for the algorithm to achieve the required distribution in a longer time as well. [18.] The OARs and their effects just mentioned earlier were skipped because they were irrelevant for the scope of this thesis work. As a conclusion, the dose distribution within the target for the purpose of clinical commissioning was considered as successful.

5.2. Delivery time and monitor units

The amount of monitor units and dose delivery time dedicated to each plan was considered to be acceptable and it increased when either the dose/fraction or target volume or both increased. In most of the cases, the gantry speed was reduced during the dose delivery. Usually in VMAT, the gantry speed is reduced when the fluence delivery is higher than what can be delivered at the maximum speed. According to Craft, [14], the gantry slows down for two reasons. First one was the very high fluence delivery, as explained earlier. The second one was the very high modulation of the fluence map [14]. Considering that the current volume was simple (sphere) and no OAR's were involved, the modulation could not be considered very complex. Therefore, the gantry speed was reduced more with higher amount of MUs to be delivered. Moreover, in this work, for better comparisons, only one (partial) arc was utilised for each case. If there were more than one, the gantry speed for each arc most likely would not be reduced, although the total treatment delivery would not change [42].

Another aspect that influences the delivery speed is also the space in degrees between the control points during the VMAT delivery. The choice of this spacing is a trade-off between the accuracy of the delivery and the delivery time. Higher the amount of control points, higher the accuracy and longer the delivery time. [43.] The control point space in the current work was 2 degrees which is considered to be a practical choice for RapidArc treatments and the delivery times noticed in the current measurements were considered clinically acceptable. Compared to 6 MV FFF SBRT VMAT delivery times of other studies with larger target volumes and similar monitor units, the current values appeared to be reasonable. For example, in Scorsetti's work [44], the FFF 6 MV beam on time ranged between 0.9 and 4.4 minutes, for doses ranging from 3.83 Gy to 12.21 Gy and dose rate of 1400 MU/min.

5.3. Dosimetric verifications with matrix detector

The most important results of the thesis were the ones related to the measurements of dose distributions. Similar pattern noticed in all of the obtained results was the disagreements between measured and calculated results in the high dose region especially when the calculated dose changed rapidly due to the high modulated fluencies. Maximal discrepancies were in most cases in the lateral horns and central area of the high dose region. However, the average discrepancies noticed in the high dose regions of the dose profiles are considered to be more important than the maximal ones. Consequently, the evaluation of the comparison between measured and calculated data was based on these average values.

According to these average discrepancy values, measured profiles were in good agreement with calculated one for PTV 6 more than for PTV 3. Average values obtained for PTV 6 in MXX-MCube setup and gantry mounted detector were 4.2 % in each case. For PTV 3, these values were 6.2 % and 6.5 %. Global averages for each setup were 5.28 % and 5.4 % for MXX-MCube and gantry mounted detector, respectively. TRS-398 standards suggested a passing threshold of 5 % and PTV 6 was the only one to be considered as acceptable in this light. Considering that this threshold is only a suggestion, global averages could be considered as quite close to the acceptance level.

Although the average disagreements of PTV 6 were within the limits, reasons of unsatisfactory results of PTV 3 and the noticed maximal discrepancies need to be investigated. Few possible reasons that could explain these differences would be the low spatial resolution of the matrix combined with angle correction factors, small field sizes and the interpolation of the calculated data.

5.3.1. Matrix spatial resolution and field size

Low spatial resolution of the matrix detector (due to the large distance between detectors) and small field sizes at the same time were considered as significant contributors to the unsatisfactory results. In principle, when steep dose changes occurred due to the high modulated fluence, the demand for better spatial resolution increased. Since the amount of ion chambers remains unchanged, the measured dose will differ from the calculated one. MXX works based on the direct measurements coming from the ion chambers and data interpolation between the chambers. Logically, interpolation is more accurate when the measured points are in a straight line or simply a larger amount of them is recorded.

Another factor that emphasized the poor detector's spatial resolution was the field size. As already mentioned, the more denser sampling recorded from the matrix, the better interpolation it performs, thus better the results. Hence, the smoother the field size, the better the outcome. This was observed in the current results where the disagreements between measured and calculated data were smaller for PTV 6 than for PTV 3. The dependency of the detector's performance on the field size can be also seen if the same detector is used for larger field sizes. In Shimohigashi's publication, [45], results between measured and calculated data obtained from the same detector were more satisfactory because the maximum square field sizes used there were 10, 15 and 20 cm which were large enough regarding the resolution [45]. Considering the actual maximum field sizes (table 4), the detector generated a low passing rate for small fields and film measurements were considered as an alternative since film's spatial resolution is considerably better.

A plausible explanation of the poor results for small field sizes could be also the linear interpolation offered from the IBA software when converting the grid. During a clinical observation concerning open fields of various sizes, it was noticed a large dis-

crepancy between measured and calculated dose levels when grid conversion was applied for very small field sizes. The doubt was on the linear interpolation of the grid size because without the applied interpolation, results were acceptable. Furthermore, it was noticed that an important factor was also the difference between the initial grid size and the final one; the smaller the difference, the smaller the discrepancies. Hence, interpolation could also explain to some extent the failures of measured dose profiles for small field sizes, especially when the dose level was not a smooth one. However, further studies in the clinic are going on to completely verify the problem.

5.3.2. Angular dependency and other factors

As it was already mentioned earlier, angular dependency is applied only for the MXX-MCube setup where the detector remains fixed and the gantry rotates around it while irradiating. It is important to consider it because detector's sensitivity is different for different angles. According to Shimohigashi, [45], angular dependency is thought to be as a result of the perturbations happening at the interface between air and high-Z material and if it is not corrected, the measured dose would be underestimated with about 3 % [45]. Also Boggula et al. [46], concluded that angle correction factor application for VMAT quality assurance improves the agreement by 4.3 % for gamma criteria of 2 %, 2 mm and even larger improvements for gamma criteria of 3 % and 3 mm. Hence, in the current measurements, angle correction factors were regarded as necessary to be applied as well.

On the other hand, angle correction factors may also be considered to have their own contribution for the unsatisfactory agreements between the data. When MXX is used before the comparison with the calculated data, angle correction factors provided by the manufacturer were applied to the measured data. Although these values were considered to work well, different publications showed that there was room for further improvement. For instance, in Feygelman's work, [43], these values were modified and results improved by 1.6 % for the 3 %, 3 mm gamma criteria. With regard to results coming from the setup with the detector mounted on the gantry, angular dependency was null because the beam was all the time perpendicular to the detector. Theoretically, the disagreements for gantry mounted results were expected to be lower than in MXX-MCube setup. However, based on the average values from the dose difference verifications, this did not seem to be the case. Two major reasons for this could be the sag between the fixation frame of the detector mounted in the gantry and secondly, the larger amount of non smooth areas in the calculated profiles for the gantry mounted detector cases. After the current measurements were completed, a sag up to 2 mm from the matrix frame of the clinic was observed and that could have dominated the angular dependency. Moreover, the different days those measurements were performed and potential drifts in calibration could have affected the final results [46]. However, it was noticed that these calibration drifts were within 1 %.

Other possible factors

An additional explanation for the differences between measured and calculated data, although in a smaller scale, was thought to be the dose distribution within the PTV. For example, in figure 22, the calculated profile is not as Gaussian as the measured profile. It seemed that if this curve would have had more regular shape, the differences would have been smaller. The grid resolution of AAA algorithm was improved from 2.5 mm to 1 mm to see if dose distribution would get more uniform and consequently the calculated profile would become more Gaussian, but that was not the case. This fact hinted that the matrix detector was better suited for dose levels measured in flat areas and the measurement of the round or pointy areas were limited due to the detector's poor resolution.

Moreover, small field sizes pose a challenge to the AAA algorithm as shown in a study related to VMAT lung treatment. The other uncertainty coming from the use of small field sizes is related to the radiation dosimetry [47]. It has been proven that small fields are challenging to the dosimetry because they cause unstable conditions due to the secondary electron track lengths and the detector size which is comparable to the field size [48]. The combination (or not) of these uncertainties can be added to the uncertainties list responsible for the disagreements in the high dose regions of calculated and measured profiles.

5.3.3. Future work

To minimize the errors coming from the mentioned sources, one could consider some future studies. At the moment, the department is working on the beam modeling modifications in order to improve the calculation accuracy, especially for small fields. Based on some studies done in another clinic with regard to the use of IMRT technique for SBRT treatments, it was noticed that the gap between measured and calculated results was smaller for leaf transmission factor of 1.6 instead of 1.0 which was used in the current work. Hence, significant improvements are expected on fine tuning of the beam model. In addition, beam data configuration was rechecked. According to Eclipse results coming from the comparison of calculated and measured data performed in water, there were no discrepancies found in the high dose region.

With regard to low spatial resolution of the matrix, Poppe [34.], proposed a technique which may improve the matrix performance. Even though it was applied on a PTW 2D array (type 10017; PTW-Freiburg, Germany) with even lower resolution than the MatriXX^{Evolution} the idea is worth exploring. This technique was based on a convolution correction technique which includes the response function of each detector. In brief, the calculated dose was convolved with the response function of an individual chamber of the matrix. Then the comparison between the obtained outcome and the measured

array signals was made. According to the author, this method would avoid most of the errors coming from the limited resolution of the matrix. [34.]

A similar study on a MatriXX detector was made and satisfactory improvements were achieved. To compare the measured and calculated data, the calculated data were corrected by its convolution with the determined response function. Equation 12 is used for data correction in one direction, where $M(x_0)$ is the signal of the matrix at point x_0 , $f(x_i)$ is the calculated signal and $g(x_0 - x_i)$ is the response function for discrete measurement points.

$$M(x_0) = \frac{\sum_{i=1}^n f(x_i) * g(x_0 - x_i)}{\sum_{i=1}^n g(x_0 - x_i)} \quad (12)$$

For the 2D correction, a rotation-symmetric response function was created and the separation of the individual ion chambers was ignored. Moreover, the resolution of calculated dose distribution was 0.076 cm compared to the measuring grid of 0.76 cm. The outcome generated by the convolution was a 32x32 matrix of single dose values, which were compared with the measured values. The disadvantages of such technique for the current results in the thesis were: the correction process did not apply for angular dependent dose deliveries such as VMAT because it was designed for IMRT at 0 degree angle and secondly, existing OmniPro I'mRT software did not support the comparison of such corrected data with the measured ones. Nonetheless, more investigations for modifying the correction formula for VMAT data would help to minimize the low matrix resolution effect on the resulted dissimilarities. [49.] In addition, other dosimetric characteristics of the existing matrix detector, such as its stability, dose linearity, dose rate response and energy dependence need to be verified particularly for FFF beams [45]. Knowing more about these aspects would help to better understand the behavior of the detector in similar situations as in the current one.

With regard to the angular correction factors, Boggula et al. [46], investigated the feasibility of matrix detector for VMAT plans for similar geometries: with MCube phantom and mounted on the gantry. The author compared results between single correction factors used for each ionization chamber of the matrix with developed correction factors for every single ion chamber. The study managed to develop these individual correction factors and noticed significant improvements. [46.] Although it has created the correction factors with different software, algorithms and equipments compared to the ones used in this thesis, the idea is an interesting one. Although it may require long time it can be considered as a future work for the department because results presented in the publication seemed promising, especially for small field sizes.

Another approach would be comparing the measurements with other the matrix detector. One example can be the PiXel-segmented ionization chamber (PXC) which has similar features as MXX, 1024 ionization chambers arranged in a 32x32 grid. The diameter of each chamber is 0.4 cm and height 0.55 cm with a distance 0.75 cm from each other and sensitive volume of 0.7 cm³. According to Stasi et al. [49], the detector performs quite well for IMRT plans judging from the outcomes of the output factors, gamma analysis and other evaluation methods [50]. Although it is tested for IMRT only, it would be a good alternative to test it for VMAT as well. Finally, the absolute dosimetry equipments can be also used to measure the smooth calculated dose.

To eliminate every possible error source, the main components of VMAT delivery need to be checked. These main components are the dose rate, gantry speed and dynamic MLCs [51]. Verification of the accuracy of these parameters and especially their combination needs to be done. For instance, the dynamic-MLC behavior and the rotational functionality need to be verified individually and in combination. Moreover, the interleaf leakage needs a double check. It influences the dose delivery inaccuracy with the same magnitude as itself. [43.]

5.4. Dosimetric verifications with film measurements

Results from the radiochromic films were partially satisfactory. The shape of measured profile was in very good agreement with the calculated one. This was considered as an important result because this was the major problem in matrix detector's results. Consequently, it demonstrated that indeed one of the key reasons of the disagreement between measured and calculated data was due to the detector's limitation and small field sizes.

On the other hand, the unsatisfactory part was the large gap between calculated and measured doses, as can be seen from figure 37. On a positive note, this aspect was proven to be correct from the detector's measurement which implied that this unsatisfactory result in the film measurements was due to film technical issues. Thus, some explanations on what might have influenced such result are given next.

In general, when doing radiochromic film measurements there are few uncertainty sources that have to be considered. According to their sources, uncertainties are classified into two main groups: inaccuracies from *calibration process* and from *dose measurements*. Inaccuracies coming from the calibration can be from the beam delivery and from the calibrated film itself (for example film in-homogeneities). As for the uncertainties coming from dose measurements, the imprecision could come from the calibration curve, irradiated film and/or post-irradiation processes (room temperature, film developing time, age of the film).[52.]

Keeping in mind these sources, it was natural to investigate all of them regarding to the current measurements. The calibration process was reconsidered and was concluded that it was correct because the relevant recommendations (as described in section 3.5.1) based on approved guidelines were followed together with the medical physicists of the department. Regarding the post-irradiation processes, the film was stored in a dark box, in room temperature, for 18 hours which were considered as optimal conditions according to Casanova et al. and Andres [35; 36]. As for the quality of the film, Casanova et al. and Reinhardt, [35; 53], proved that the current film was a feasible one for IMRT quality assurance and its overall inaccuracies would not exceed 2 %. These inaccuracies would be the film non-homogeneity, fit accuracy, intra-batch variations and artefacts generated from the scanner [34; 52]. Moreover, new measurements with new films and new calibration curves were performed and again the difference between the data sets was significant and unacceptable. Therefore, keeping in mind that the mentioned inaccuracies would sum up only for about 2 %, there is still a large percentage of inaccuracy that cannot be explained, yet.

5.4.1. Future work

Some future work that can be done for improving the inaccuracies mentioned earlier is by investigating if there is any correlation between the results of the film and the ones from the MXX-MCube. It was an interesting fact that for the same plan, PTV 3 and dose/fraction of 4 Gy, the film and the MXX-MCube measurements had similar disagreements ranging from 8-10 %, in the Y-direction. If such correlation exists, this could hint that there may be an uncertainty with either the beam delivery or with the TPS calculations; the last one being most likely the issue.

Another aspect to be considered is to use film dosimetry starting with the simplest plans and dose distributions that need no complex beam modulation, for example open fields. If the results are successful, then it can be preceded with more complex plans. This would ensure that film quality, film calibration and dose delivery are correct.

To minimize any possible erroneousess regarding the film, one could also work on the calibration curve by developing or using a more complex equation that generates such curve. However, one must be careful with this modification because the more complex the equation, the more parameters involved, thus uncertainty increases [52]. Furthermore, another relatively important flaw of the film that could influence the results for absolute dosimetry is the heterogeneity within the same film and inter-batch variations, due to the manufacturing process. One could avoid the inter batch variations by using films from the same batch only and the same scanning device which was the case in this study. Finally, as for the heterogeneity, one could tackle it by scanning multiple films and taking their average as the measured data [8].

6. CONCLUSION

In this thesis, the aim was clinical commissioning of flattening filter free (FFF) 6 MV photon beam for stereotactic body radiation therapy (SBRT) volume modulated arc therapy (VMAT) lung treatment. This was done by creating two different spherical target volumes with diameters 3 cm (PTV 3) and 6 cm (PTV 6) and four radiotherapy plans with different prescribed doses. Dose distribution within the PTVs was planned according to RTOG protocol. Then the treatment plans were transferred to cubic solid water phantom. Two techniques were used to assess the difference between measured and calculated dose distributions: 2D ionization chamber matrix detector and radiochromic film.

Results obtained from the matrix detector were partially satisfactory because the dose level of measured and calculated dose profiles were in good agreement for PTV 6 only. The average disagreement was in every plan of PTV 6 within the accuracy criterion suggested by technical reports series (TRS) 398. Based on the same evaluation protocol, PTV 3 was not acceptable. Furthermore, the disagreement was smaller when the matrix was on the treatment couch than when it was placed on gantry holder. This is most likely because of the sag between the fixation frame and the detector. Going in more details, in every measurement the highest disagreements were in the regions where the calculated profile had rapid dose level changes. The failure of the detector to correctly measure these areas was thought to be mainly due to its low spatial resolution combined with small field sizes and the challenge that small field sizes introduce to the dose calculation algorithm. There were also deviations in overall dose levels. Future studies related to these problems are required and the department is currently working on to fine tune the beam modelling used for the dose calculation of small fields.

Results from the film measurements showed that the measured dose profile matched almost perfectly with the calculated profile. It was a crucial outcome considering that this was the main problem in the detector measurements. The only reason making the film measurement partly successful was the large gap in dose levels between measured and calculated dose profiles. That did not exist with the matrix detector. Consequently, this gap seen on film measurement was thought to be mainly due to the inaccuracies coming either from film calibration process or post-irradiation film process. Further studies on these issues are also necessary and the department has already started them.

As a final remark, based on the results obtained with the matrix detector and radiochromic film, the commissioning of the 6 MV FFF beam for SBRT lung treatment is considered as partly successful. This means that the shape of the dose distributions can be accurately calculated but there exist unacceptable dose level deviations for very small target volumes. Before FFF 6 MV beams are clinically used, studies concerning the main problems mentioned earlier are needed and additional measurements for different modulated beams are required.

7. REFERENCES

[1] Williams, J. R., Thwaites, D. I. Radiotherapy Physics in Practice. Oxford University Press, 2000.

[2] Benedict, S. H., Yenice, K. M., Followill, D., Galvin, J. M., Hinson, W., Kavanagh, et. al. "Stereotactic body radiation therapy: The report of AAPM Task Group 101" Med. Phys., vol. 37, pp. 4078-4101, 08, 2010.

[3] RTOG-0618. "A phase II trial of stereotactic body radiation therapy (SBRT) in the treatment of patients with operable stage I/II non-small cell lung cancer". Radiation Therapy Oncology Group, USA, 2010.

[4] Ong, C. L., Verbakel, W. F. A. R., Dahele, M., Cuijpers, J. P., Slotman, B. J., Senan, S. "Fast Arc Delivery for Stereotactic Body Radiotherapy of Vertebral and Lung Tumors". International Journal of Radiation Oncology*Biophysics, vol. 83, pp. e137-e143, 5/1, 2012.

[5] World Health Organization, (January 2013). Cancer. Available: <http://www.who.int/mediacentre/factsheets/fs297/en/index.html>.

[6] Podgorsak, E. B. Radiation Oncology Physics: A Handbook for Teachers and Students. Vienna, Austria: IAEA, 2005.

[7] Taylor, A., Powell, M. E. "Intensity-modulated radiotherapy--what is it?" PubMed, vol. 4, pp. 68, 2004.

[8] David I Thwaites and John, B.Tuohy. "Back to the future: the history and development of the clinical linear accelerator". Phys. Med. Biol., vol. 51, pp. R343, 2006.

[9] Raaymakers, B. W., Raaijmakers, A. J. E., Kotte, A. N. T. J., Jette, D., Lagendijk, J.J.W. "Integrating a MRI scanner with a 6 MV radiotherapy accelerator: dose deposition in a transverse magnetic field". Phys. Med. Biol., vol. 49, pp. 4109, 2004.

[10] Greene, D. Linear Accelerators for Radiation Therapy. UK: Adam Hilger Ltd, 1986.

[11] Kahn, F. M. The Physics of Radiation Therapy. USA: Wolters Kluwer|Lippincott William & Wilkins, 2012.

[12] Varian Medical Systems. "Eclipse reference guide: Treatment planning for external beam". Varian Medical Systems, Finland, 2010.

- [13] Ezzell, A., G., Galvin, M., J., Low, D., Palta, R., J., Rosen, I., Sharpe, B., et al. "Guidance document on delivery, treatment planning, and clinical implementation of IMRT: Report of the IMRT subcommittee of the AAPM radiation therapy committee". *Med. Phys.*, vol. 30, pp. 2089, 2003.
- [14] Craft, D., McQuaid, D., Wala, J., Chen, W., Salari, E., Bortfeld, T. "Multicriteria VMAT optimization". *Med. Phys.*, vol. 39, pp. 686, 2012.
- [15] Ding, L., Lo, Y. C., Kadish, S., Goff, D., Pieters, R. S., Graeber, G. "Volume Modulated Arc Therapy (VMAT) for pulmonary Stereotactic Body Radiotherapy (SBRT) in patients with lesions in close approximation to the chest wall". *PubMed*, vol. 3, pp. 12, 2013.
- [16] RTOG-0915. "A randomized phase II study comparing 2 stereotactic body radiation therapy (SBRT) schedules for medically inoperable patients with stage I peripheral non-small cell lung cancer". Radiation Therapy Oncology Group, USA, 2009.
- [17] Timmerman, R., Heinzerling, J., Abdulrahman, R., Choy, H., Meyer, J. L. "Stereotactic body radiation therapy for thoracic cancers: recommendations for patient selection, setup and therapy". vol. 43, pp. 395, 2011.
- [18] Holt, A., van Vliet-Vroegindeweij, C., Mans, A., Belderbos, J. S., Damen, E. M. F. "Volumetric-modulated arc therapy for stereotactic body radiotherapy of lung tumors: A comparison with intensity-modulated radiotherapy techniques". *International Journal of Radiation Oncology*Biography*Physics*, vol. 81, pp. 1560-1567, 12/1, 2011.
- [19] Sharma, S. D. "Unflattened photon beams from the standard flattening filter free accelerators for radiotherapy: Advantages, limitations and challenges". *Journal of Medical Physics*, vol. 36, pp. 123-125, Jul, 2011.
- [20] Ting, J. "Commissioning of varian TrueBeam with flattening filter free: FFF design". Florida, USA: MIMA Cancer Center / Global Physics Solutions, pp. 98.
- [21] Lang, S., Reggiori, G., Vaque, J. P., Calle, C., Hrbacek, J., Klock, S., et al. "Pre-treatment quality assurance of flattening filter free beams on 224 patients for intensity modulated plans: A multicentric study". *Med. Phys.*, vol. 39, pp. 1351-1356, 2012.
- [22] Ting, J. "MO-A-BRB-02: Facts and fiction of flattening filter free (FF-FFF) X-rays beams". in 2012, pp. 3861-3862.
- [23] Wang, L., Mok, E., Xing, L. "TU-B-BRA-03: Pros and cons of flattening filter free IMRT: A comparison with conventional IMRT with flattened beams". 2010, pp. 3375-3375.
- [24] Lalonde, R. (April 18th, 2011). To flatten or not to flatten?. Available: <http://www.lalondemedphysics.com/2011/04/18/to-flatten-or-not-to-flatten/>

- [25] Dyk, V. J., Barnett, R. B., Battista, J. J. "Computerized radiation treatment planning systems". *Modern Technology of Radiation Oncology: A Compendium for Medical Physicists and Radiation Oncologists*, Dyk, V. J. ed. Medical Physics Publishing, 1999, pp. 232.
- [26] Varian Medical Systems. "Eclipse algorithms reference guide: Eclipse". Varian Medical Systems, Finland, 2010.
- [27] Esch, A. V., Tillikainen, L., Pyykkonen, J., Tenhunen, M., Helminen, H., Siljamaki, S., Alakuijala, J., Paiusco, M., Iori, M., Huyskens, D. P. "Testing of the analytical anisotropic algorithm for photon dose calculation". *Med. Phys.*, vol. 33, pp. 4130-4148, 2006.
- [28] Stern, R. L., Heaton, R., Fraser, M. W., Murty Goddu, S., Kirby, T. H., Lam, K. L., Molineu, A., Zhu, T. C. "Verification of monitor unit calculations for non-IMRT clinical radiotherapy: Report of AAPM Task Group 114". *Med. Phys.*, vol. 38, pp. 504-530, 01, 2011.
- [29] Lagerwaard, F. J., Haasbeek, C. J. A., Smit, E. F., Slotman, B. J., Senan, S. "Outcomes of Risk-Adapted Fractionated Stereotactic Radiotherapy for Stage I Non-Small-Cell Lung Cancer". *International Journal of Radiation Oncology*Biography*Physics*, vol. 70, pp. 685-692, 3/1, 2008.
- [30] Hurkmans, C., Cuijpers, J., Lagerwaard, F., Widder, J., van, d. H., Schuring, D. , Senan, S. "Recommendations for implementing stereotactic radiotherapy in peripheral stage IA non-small cell lung cancer: report from the Quality Assurance Working Party of the randomised phase III ROSEL study". *Radiation Oncology*, vol. 4, pp. 1, 2009.
- [31] Saminathan, S., Manickam, R., Chandraraj, V., Supe, S. "Dosimetric study of 2D ion chamber array matrix for the modern radiotherapy treatment verification". *PubMed*, vol. 11, pp. 3076, 2010.
- [32] Chandraraj, V., Stathakis, S., Manickam, R., Esquivel, C., Supe, S., Papanikolaou, N. "Comparison of four commercial devices for RapidArc and sliding window IMRT QA". *PubMed*, vol. 12, pp. 3367, 2011.
- [33] IBA Dosimetry GmbH. "OmniPro I'mRT System Version 1.7b: User's guide". Germany, 2010.
- [34] Poppe, B., Blehschmidt, A., Djouguela, A., Kollhoff, R., Rubach, A., Willborn, K. C., Harder, D. "Two-dimensional ionization chamber arrays for IMRT plan verification". *Med. Phys.*, vol. 33, pp. 1005-1015, 2006.
- [35] Casanova, B. V., Pasquino, M., Russo, G., Grosso, P., Cante, D., Sciacero, P. et al. "Dosimetric characterization and use of GAFCHROMIC EBT3 film for IMRT dose verification". *Journal of Applied Clinical Medical Physics*, vol. 14, 2013.
- [36] Andrés, C., del Castillo, A., Tortosa, R., Alonso, D., Barquero, R. "A comprehensive study of the Gafchromic EBT2 radiochromic film. A comparison with EBT". *Med.Phys.* vol. 37, pp. 6271-6278, 12, 2010.

- [37] Aland, T., Kairn, T., Kenny, J. "Evaluation of a Gafchromic EBT2 film dosimetry system for radiotherapy quality assurance". *Pub. Med.* vol. 34, pp. 251, 2011.
- [38] Low, D. A., Dempsey, J. F. "Evaluation of the gamma dose distribution comparison method". *Med. Phys.*, vol. 30, pp. 2455-2464, 2003.
- [39] Low, D. A., Harms, W. B., Mutic, S., Purdy, J. A. "A technique for the quantitative evaluation of dose distributions". *Med. Phys.*, vol. 25, pp. 656-661, 1998.
- [40] "Descriptors of dose distributions". Available:
<http://ozradonc.wikidot.com/descriptors-of-dose-distribution-photons>
- [41] International Atomic Energy Agency. "Absorbed dose determination in external beam radiotherapy: an international code of practice for dosimetry based on standards of absorbed dose to water". Vienna, Austria: IAEA, 2000.
- [42] Zwahlen, D. R., Lang, S., Hrbacek, J., Glanzmann, C., Kloeck, S., Najafi, Y. et al. "The Use of Photon Beams of a Flattening Filter-free Linear Accelerator for Hypofractionated Volumetric Modulated Arc Therapy in Localized Prostate Cancer". *International Journal of Radiation Oncology*Biology*Physics*, vol. 83, pp. 1655-1660, 8/1, 2012.
- [43] Feygelman, V., Zhang, G., Stevens, C. "Initial dosimetric evaluation of SmartArc - a novel VMAT treatment planning module implemented in a multi-vendor delivery chain". *PubMed*, vol. 11, pp. 3169, 2010.
- [44] Scorsetti, M., Alongi, F., Castiglioni, S., Clivio, A., Fogliata, A., Lobefalo, F. "Feasibility and early clinical assessment of flattening filter free (FFF) based stereotactic body radiotherapy (SBRT) treatments". *Radiation Oncology*, vol. 6, pp. 113, 2011.
- [45] Shimohigashi, Y., Araki, F., Tominaga, H., Sakata, J., Kawasaki, K., Kanetake, N. et al. "Angular dependence correction of MatriXX and its application to composite dose verification". *Journal of Applied Clinical Medical Physics*, vol. 13, 2012.
- [46] Boggula, R., Birkner, M., Lohr, F., Steil, V., Wenz, F., Wertz, H. "Evaluation of a 2D detector array for patient-specific VMAT QA with different setups". *Phys. Med. Biol.*, vol. 56, pp. 7163, 2011.
- [47] Seppala, J., Suilamo, S., Kulmala, J., Pekka, M., Minn, H. "A dosimetric phantom study of dose accuracy and build-up effects using IMRT and RapidArc in stereotactic irradiation of lung tumors". *Radiation Oncology*, vol. 7, pp. 77, 2012.
- [48] Das, J., I., Ding, X., G., Ahnesjo, A., "Small fields: nonequilibrium radiation dosimetry". *Med. Phys.*, vol. 35, pp. 206, 2007.
- [49] Herzen, J., Todorovic, M., Cremers, F., Platz, V., Albers, D., Bartels, A., Schmidt, R. "Dosimetric evaluation of a 2D pixel ionization chamber for implementation in clinical routine". *Phys. Med. Biol.*, vol. 52, pp. 1197, 2007.

[50] Stasi, M., Giordanengo, S., Cirio, R., Boriani, A., Bourhaleb, F., Cornelius, I. et al. "D-IMRT verification with a 2D pixel ionization chamber: dosimetric and clinical results in head and neck cancer". *Phys. Med. Biol.*, vol. 50, pp. 4681, 2005.

[51] Ling, C. C., Zhang, P., Archambault, Y., Bocanek, J., Tang, G., LoSasso, T. "Commissioning and Quality Assurance of RapidArc Radiotherapy Delivery System" *International Journal of Radiation Oncology*Biophysics*, vol. 72, pp. 575-581, 10/1, 2008.

[52] Devic, S. "Radiochromic film dosimetry: Past, present, and future". *Physica Medica*, vol. 27, pp. 122-134, 7, 2011.

[53] Reinhardt, S., Hillbrand, M., Wilkens, J. J., Assmann, W. "Comparison of Gafchromic EBT2 and EBT3 films for clinical photon and proton beams". *Med. Phys.*, vol. 39, pp. 5257-5262, 2012.